University of Padova

Department of Physics and Astronomy "Galileo Galilei"

Master Thesis in Physics of Data

Design and characterization of a light-tight, compact magnetic shield for superconducting qubits

Internal Supervisor
Caterina Braggio
University of Padova

External supervisor
Alexandre May
Quantronics group – CEA, SPEC

Master Candidate
Alessandro Miotto

Student ID
2139205

Academic Year
2025-2026

Abstract

A light-tight magnetic shield is essential for protecting superconducting circuits, as these devices are extremely sensitive to external magnetic fields and stray electromagnetic radiation. Even minimal magnetic flux or light leakage can break Cooper pairs, induce quasiparticles, and introduce noise or decoherence, significantly degrading circuit performance.

Designing a shield that combines high magnetic permeability with opacity at microwave, optical, and infrared frequencies allows for the suppression of ambient magnetic fields while preventing photon-induced excitations, ensuring stable superconducting operation.

The characterization of such a shield by measuring its magnetic field attenuation, light leakage, and thermal compatibility at cryogenic temperatures, is fundamental to verify that it meets the strict requirements for superconducting circuit experiments.

Contents

1 Introduction

Superconducting circuits have emerged as a highly versatile platform for the physical implementation of quantum technologies. Benefiting from the maturity of microwave engineering and scalable microfabrication techniques, these devices are central not only to quantum computing and information processing but also to quantum sensing. Operating in the microwave frequency domain, superconducting sensors offer exceptional sensitivity, enabling applications ranging from electron spin resonance detection in solids [1, 2] to fundamental physics research [3], such as high-frequency gravitational waves [4] and dark matter axions [5, 6]. However, this extreme sensitivity inherently results in a high susceptibility to environmental noise [7]. To preserve quantum coherence and ensure reliable operation, it is strictly necessary to isolate these circuits from their external environment.

This thesis presents research conducted during a four-month internship at the Quantronics group (SPEC, CEA Paris-Saclay), focusing on the comprehensive shielding of superconducting circuits, particularly on single microwave photon detectors (SMPD) [8]. In many sensing applications, the devices must operate in proximity to strong magnetic fields, where uncontrolled magnetic flux can degrade the performance of superconducting components. To contextualize these challenges, Chapter 2 outlines the fundamental principles of superconductivity, while Chapter 3 provides a theoretical review of superconducting qubits. Building on this foundation, Chapter 4 details the design and evaluation of a compact, multilayer magnetic shield. This section includes finite element method (FEM) simulations to model the magnetic attenuation provided by combining high-permeability ferromagnetic materials with both Type I and Type II superconducting layers.

In addition to magnetic interference, superconducting circuits are vulnerable to pair-breaking radiation. Ambient infrared photons can generate non-equilibrium quasiparticles, which constitute a primary decoherence channel. Quasiparticle tunneling reduces the energy relaxation time of the qubits and increases the dark count rate in sensing applications [9, 10]. Chapter 5 focuses on mitigating this specific noise source through environmental shielding. Strategies to achieve strict light-tightness are discussed, including the use of interlocking mechanical designs, infrared-absorbing coatings, and in-line microwave filters. Although fabrication time constraints prevented a full experimental characterization within the internship period, a testing protocol utilizing offset-charge-sensitive (OCS) qubits is presented to quantitatively evaluate the efficacy of the shielding against stray photon leakage [11].

Finally, the concept of shielding is broadened in Chapter 6 to include the protection of the quantum state from the control and measurement apparatus itself. During standard dispersive readout, increasing the photon population inside the readout resonator improves the signal-to-noise ratio but can simultaneously invalidate the dispersive approximation [12]. This breakdown leads to measurement-induced state transitions (MIST), where the qubit undergoes spurious excitations and ionization due to non-trivial multi-photon resonances. Chapter 6 investigates these parametric processes using both quantum branch analysis and semi-classical Floquet simulations. By applying this computational framework to a single microwave photon detector, the study provides a methodology to map the safe operational parameter space, guiding future circuit design to avoid measurement-driven decoherence.

2

Superconductivity

The phenomenon of superconductivity was first discovered in 1911 by H. K. Onnes [13], who observed that the electrical resistance of various metals drops to zero when cooled below a material-specific critical temperature T_c. Subsequent experiments demonstrating the existence of persistent currents inside superconducting rings provided further evidence of this dissipationless state. In 1933, Meissner and Ochsenfeld [14] observed that superconductors also exhibit perfect diamagnetism: when some materials are cooled below T_c in the presence of an external magnetic field, the field is actively expelled from the bulk.

In this chapter, we introduce the theoretical frameworks required to understand the phenomena of superconductivity. We begin with the macroscopic electrodynamic description developed by the London brothers in Section 2.1. This model provides the justification for treating superconducting shields as perfect diamagnets and establishes the range of validity for the shielding models presented in Chapter 4. In Section 2.2, the Ginzburg-Landau theory is introduced to explain the thermodynamics of the phase transition, the emergence of Type II superconductivity, and the dynamics of flux vortices, which are central to the performance of superconducting circuits. Finally, in Section 2.3, the microscopic Bardeen-Cooper-Schrieffer (BCS) theory is briefly reviewed.

2.1 London equations

Following the experimental observations of Onnes and Meissner, the first successful phenomenological description of superconducting electrodynamics was proposed by F. and H. London in 1935 [15]. Their model assumes that a fraction of the conduction electrons, denoted by a super-carrier density n_s, participate in the dissipationless supercurrent [16]. Applying the Drude model in the absence of scattering (zero resistance), the acceleration of these superconducting carriers of mass m and charge e in an electric field $\mathbf{E}$ is given by $d\mathbf{v}_s/dt = e\mathbf{E}/m$. This expression yields the time evolution of the supercurrent density:

$$\frac{d\mathbf{J}_s}{dt} = \frac{n_s e^2}{m}\mathbf{E}. \tag{2.1}$$

This relation is known as the first London equation. It captures the zero-resistance property, showing that any applied electric field will continuously accelerate the charge carriers, in contrast to the steady drift velocity described by Ohm's law in normal metals.

To capture the Meissner effect, we take the curl of Equation 2.1 and substitute Faraday's law of induction, $\nabla \times \mathbf{E} = -\partial\mathbf{B}/\partial t$. This yields the second London equation:

$$\nabla \times \mathbf{J}_s = -\frac{n_s e^2}{m}\mathbf{B}. \tag{2.2}$$

By inserting this result into Ampère's law, we obtain an Helmholtz equation that describe the magnetic field inside the superconductor: $\nabla^2\mathbf{B} = \mathbf{B}/\lambda_s^2$, where $\lambda_s = \sqrt{m/\mu_0 n_s e^2}$ is defined as the London penetration depth. The exponential decay of the solution $\mathbf{B}(x) = \mathbf{B}(0)e^{-x/\lambda_s}$ explains the Meissner effect, demonstrating that magnetic fields are not strictly discontinuous at the surface but rather penetrate the superconductor over a characteristic distance λ_s.

For standard superconducting materials, the typical value of λ_s is on the order of 100 nm. Because this penetration depth is orders of magnitude smaller than the thickness of our macroscopic magnetic shields (which are typically on the order of 1 mm), we can safely employ a perfect diamagnet approximation ($\mathbf{B} = 0$ everywhere inside the bulk) for the superconducting layers. This approximation simplifies the boundary conditions and enables the analytical results derived in Chapter 4, which served as the foundation for the initial shield design.

2.2 Ginzburg-Landau theory

While the London equations successfully describe the electrodynamics of the superconducting state, they do not account for spatial variations in the supercurrent density or the thermodynamics of the phase transition. In 1950, V. Ginzburg and L. Landau [17] proposed a model that describes the superconducting electrons using a complex pseudo-wavefunction $\psi(\mathbf{r})$, acting as the order parameter of the transition. The local density of superconducting carriers, herein treated as a condensate, is given by $n_s = |\psi(\mathbf{r})|^2$.

According to GL theory, near the critical temperature T_c, the free energy density of the superconducting state f_s can be expanded in a series of powers of the order parameter. Using Gaussian units, the expansion around the normal state free energy f_n takes the form:

$$f_s - f_n = \alpha|\psi|^2 + \frac{1}{2}\beta|\psi|^4 + \frac{1}{2m^*}\left|\left(-i\hbar\nabla - \frac{e^*}{c}\mathbf{A}\right)\psi\right|^2 + \frac{\mathbf{H}^2}{8\pi}, \tag{2.3}$$

Here, e^* and m^* denote the effective charge and mass of the supercurrent carriers (subsequently identified by BCS theory as Cooper pairs, such that $e^* = 2e$ and $m^* = 2m$). The first term represents the energy associated with the condensate density, contributing an energy α per unit volume, while the quartic term describes the self-interaction of the condensate with a magnitude of $\beta/2$. The third term accounts for the kinetic energy of the carriers, incorporating both the canonical momentum operator $\hat{\mathbf{p}} = -i\hbar\nabla$ and the minimal coupling to the magnetic vector potential $\mathbf{A}$. The final term represents the energy stored in the magnetic field $\mathbf{H}$. An electric field contribution is omitted because the presence of a steady supercurrent enforces $\mathbf{E} = 0$, in accordance with the first London equation.

In the absence of an applied magnetic field, the equilibrium state of the system is found by minimizing the free energy terms $f_s - f_n = \alpha|\psi|^2 + \frac{1}{2}\beta|\psi|^4$. The physical behavior of the system depends entirely on the sign of the parameters. To capture the phase transition observed by Onnes, the parameter α is defined to have a linear temperature dependence, $\alpha(T) = \alpha_0(T - T_c)$, where α_0 and β are fixed positive constants.

Consequently, for temperatures above T_c, the parameter α is positive, and the global minimum of the free energy occurs at $|\psi|^2 = 0$, corresponding to the normal resistive state. However, when the system is cooled below T_c, α becomes negative. The free energy profile develops a "Mexican hat" shape (shown in Figure 2.1), and the minimum shifts to a non-zero value

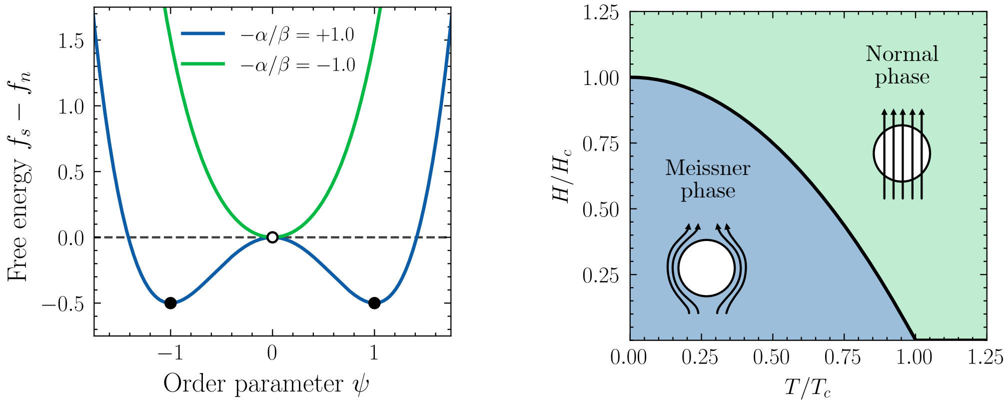

Figure 2.1: (Left) The free energy landscape as a function of the order parameter ψ for a zero-field superconductor. Depending on the sign of α, the system either possesses a single minimum at $\psi = 0$ (normal phase) or degenerate minima at a finite $|\psi|$ (superconducting phase). (Right) A temperature-magnetic field phase diagram illustrating the boundary between the normal and superconducting states.

$|\psi_{\text{eq}}|^2 = -\alpha/\beta$. This spontaneous symmetry breaking results in a finite density of superconducting carriers, marking the transition into the Meissner phase.

Substituting this equilibrium value back into the free energy expansion yields the condensation energy of the superconducting state, $f_s - f_n = -\alpha^2/2\beta$. If an external magnetic field is applied, the superconductor must spend energy to expel the field from its bulk. The superconducting state will be destroyed if the magnetic energy cost exceeds the condensation energy. Equating the two terms allows us to define the thermodynamic critical magnetic field $H_c^2 = 4\pi\alpha^2/\beta$. If the applied field exceeds H_c, it becomes energetically favorable for the material to revert to the normal state and allow the magnetic flux to penetrate uniformly.

The interplay between temperature and magnetic field defines the operational boundaries of the superconducting phase, as showed in the right panel of Figure 2.1. This thermodynamic vulnerability is one of the primary reasons why magnetic shielding is an necessity when operating superconducting circuits.

2.2.1 Type II superconductors

Minimizing the free energy in Equation 2.3 by expressing the order parameter in the polar form $\psi(\mathbf{r}) = |\psi(\mathbf{r})|e^{i\varphi(\mathbf{r})}$ yields the Ginzburg-Landau differential equation:

$$\alpha\psi + \beta|\psi|^2\psi + \frac{1}{2m^*}\left(-i\hbar\nabla - \frac{e^*}{c}\mathbf{A}\right)^2\psi = 0. \tag{2.4}$$

This relation takes the form of a time-independent Schrödinger equation for a particle of charge e^* and mass m^*, with an energy eigenvalue of $-\alpha$ and a nonlinear repulsive potential given by $\beta|\psi|^2$. The supercurrent density $\mathbf{J}$ can be computed analogously to a probability current:

$$\mathbf{J} = -\frac{ie^*\hbar}{2m^*}\left(\psi^*\nabla\psi - \psi\nabla\psi^*\right) - \frac{e^{*2}}{m^*c}|\psi|^2\mathbf{A} = \frac{e^*}{m^*}|\psi|^2\left(\hbar\nabla\varphi - \frac{e^*}{c}\mathbf{A}\right). \tag{2.5}$$

By analyzing the field-free Ginzburg-Landau equation in one dimension for a normalized wave function $f = \psi/\psi_{\mathrm{eq}}$, we identify a characteristic length scale for spatial variations in the order parameter. This Ginzburg-Landau coherence length is defined as $\xi(T) = \hbar/\sqrt{2m^*|\alpha(T)|}$, yielding the dimensionless equation:

$$\xi^2\frac{d^2f}{dx^2} + f - f^3 = 0. \tag{2.6}$$

The coherence length ξ is particularly important when considering the boundary between a superconducting region ($f = 1, H = 0$) and a normal region ($f = 0, H = H_c$).

The thermodynamic behavior of the superconductor is governed by the interplay between the magnetic penetration depth λ_s and the coherence length ξ. By defining the dimensionless Ginzburg-Landau parameter $\kappa = \lambda_s/\xi$, materials can be classified into two distinct categories:

- $\kappa < 1/\sqrt{2}$: The magnetic field penetrates the material over a distance shorter than the length required for the superconducting condensate to recover. This results in a positive surface energy at the boundary between normal and superconducting domains. The system minimizes its energy by avoiding such interfaces, resulting in the destruction of superconductivity above a critical field. This behavior defines Type I superconductors.
- $\kappa > 1/\sqrt{2}$: The surface energy becomes negative, making the formation of interfaces energetically favorable. Magnetic flux penetrates the superconductor through isolated tubes of normal phase known as Abrikosov vortices [18], where $\psi = 0$. Materials exhibiting this behavior are classified as Type II superconductors.

Because the system seeks to maximize the number of these favorable interfaces, each vortex carries one magnetic flux quantum, $\Phi_0 = hc/e^*$. Experimental measurements of this quantized flux confirm that the charge of the supercurrent carriers is $e^* = 2e$, providing evidence for electron pairing.

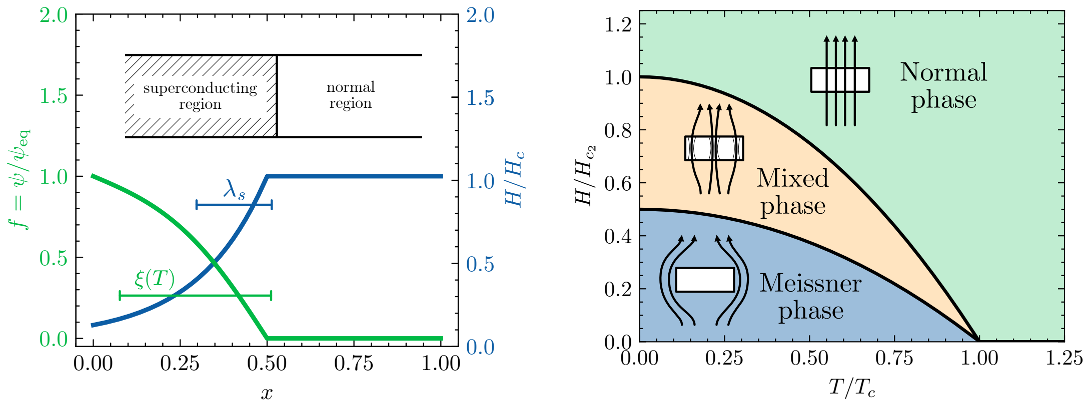

Figure 2.2: (Left) Illustration of the interplay between the superconducting coherence length ξ and the magnetic penetration depth λ_s at a superconductor-normal region interface. (Right) A temperature-magnetic field phase diagram detailing the boundaries between the normal and superconducting states. This diagram highlights the mixed phase characteristic of Type-II superconductors, where magnetic flux penetrates the material through vortices.

The formation of vortices allows Type II superconductors to enter a mixed state, where superconductivity persists in the presence of penetrating magnetic fields. Consequently, these materials exhibit two critical fields: a lower critical field H_{c1} marking the onset of vortex penetration, and an upper critical field H_{c2} where bulk superconductivity is fully destroyed. This extended resilience to strong magnetic fields makes Type II materials highly suitable for the protective shielding environments which will be discussed in Chapter 4.

2.2.2 Josephson effect

A direct application of the Ginzburg-Landau theory is the derivation of the Josephson effect [19]. Consider two bulk superconductors at equilibrium separated by a insulating barrier of length L. Within the bulk, the magnitude of the normalized order parameter approaches unity ($|f|^2 = 1$). We can write the order parameters on each side as $f_1 = e^{i\varphi_1}$ and $f_2 = e^{i\varphi_2}$. Without loss of generality, we can absorb the global phase and define the relative phase difference as $\varphi = \varphi_2 - \varphi_1$, such that $f_1 = 1$ and $f_2 = e^{i\varphi}$.

If the barrier is short compared to the coherence length ($L \ll \xi$), the gradient term in Equation 2.6 dominates, reducing the differential equation to $d^2 f/dx^2 = 0$. The solution is a linear interpolation $f(x) = a + bx$ across the junction. Applying the boundary conditions and substituting the resulting wave function into Equation 2.5 yields the current-phase relation:

$$I = I_c \sin\varphi, \tag{2.7}$$

where I_c is the critical current of the junction. Equation 2.7 demonstrates that a DC supercurrent can flow between the junction even in the complete absence of a voltage bias. In addition, applying a voltage V across the junction causes the phase difference to evolve dynamically at a rate $d\varphi/dt = 2eV/\hbar$. Together, these relations constitute a non-linear inductance, serving as the foundational element for superconducting quantum circuits.

2.3 BCS theory

In 1957, J. Bardeen, L. Cooper, and J. R. Schrieffer (BCS) [20] provided the first comprehensive microscopic theory of superconductivity. The central mechanism of BCS theory is that electrons in a metal can experience a net attractive interaction mediated by the vibrations of the underlying crystal lattice. An electron moving through the lattice slightly displaces the positively charged ions, creating a localized region of positive charge that attracts a second electron. When this phonon-mediated attraction overcomes the Coulomb repulsion, the electrons bound together to form a Cooper pair.

Because the total momentum of the ground state condensate must be zero, the pairing occurs between electrons with equal and opposite momenta ($\mathbf{k}$ and $-\mathbf{k}$) and opposite spins ($\uparrow$ and $\downarrow$). The BCS pairing Hamiltonian can be expressed as:

$$H_{\text{BCS}} = \sum_{\mathbf{k}\sigma} \xi_{\mathbf{k}} \hat{c}^\dagger_{\mathbf{k}\sigma} \hat{c}_{\mathbf{k}\sigma} + \sum_{\mathbf{k}\mathbf{k}'} V_{\mathbf{k}\mathbf{k}'} \hat{c}^\dagger_{\mathbf{k}\uparrow} \hat{c}^\dagger_{-\mathbf{k}\downarrow} \hat{c}_{-\mathbf{k}'\downarrow} \hat{c}_{\mathbf{k}'\uparrow}. \tag{2.8}$$

The first term accounts for the kinetic energy of the normal electrons, where $\xi_{\mathbf{k}} = \hbar^2 k^2/2m - \varepsilon_F$ is the energy relative to the Fermi level, and the ladder operators $\hat{c}^\dagger_{\mathbf{k}\sigma}$ and $\hat{c}_{\mathbf{k}\sigma}$ respectively create and annihilate an electron with momentum $\mathbf{k}$ and spin σ. The second term represents the scattering process responsible for Cooper pair formation, coupling paired states with initial momenta $\pm\mathbf{k}'$ to final momenta $\pm\mathbf{k}$ through an interaction potential $V_{\mathbf{k}\mathbf{k}'}$.

2.3.1 Quasiparticles

While a complete derivation of macroscopic superconducting properties from BCS theory is beyond the scope of this thesis (see Reference [16] for an extensive treatment), we briefly outline the concept of quasiparticle excitations. Understanding these excitations is critical for analyzing the decoherence mechanisms in superconducting qubits and motivates the mitigation strategies presented in Chapter 5.

By treating the interaction in a mean-field approximation, we define the superconducting energy gap $\Delta_{\mathbf{k}} = -\sum_{\mathbf{k}'} V_{\mathbf{k}\mathbf{k}'} \langle \hat{c}_{-\mathbf{k}'\downarrow} \hat{c}_{\mathbf{k}'\uparrow} \rangle$. This parameter quantifies the energy gained by condensing paired electrons relative to the normal state. The BCS Hamiltonian can then be diagonalized using a Bogoliubov transformation, which yields an effective non-interacting Hamiltonian:

$$H_{\mathrm{BCS}}^{\mathrm{eff}} = \sum_{\mathbf{k}} (\xi_{\mathbf{k}} - E_{\mathbf{k}} + \Delta_{\mathbf{k}} \langle \hat{c}_{-\mathbf{k}\downarrow} \hat{c}_{\mathbf{k}\uparrow} \rangle) + \sum_{\mathbf{k},\sigma} E_{\mathbf{k}} \hat{\gamma}_{\mathbf{k}\sigma}^{\dagger} \hat{\gamma}_{\mathbf{k}\sigma}. \tag{2.9}$$

The first term is a constant representing the macroscopic energy of the superconducting ground state. The second term describes single-particle excitations out of this condensate, known as Bogoliubov quasiparticles. These excitations are governed by the fermionic creation and annihilation operators $\hat{\gamma}_{\mathbf{k}\sigma}^{\dagger}$ and $\hat{\gamma}_{\mathbf{k}\sigma}$.

The energy spectrum for these quasiparticles is given by $E_{\mathbf{k}} = (\xi_{\mathbf{k}}^2 + |\Delta_{\mathbf{k}}|^2)^{1/2}$. Consequently, the parameter $\Delta_{\mathbf{k}}$ dictates the minimum energy required to break a Cooper pair and create a quasiparticle excitation, acting as a gap in the density of states. In the limit where $T \to T_c$, the gap vanishes ($\Delta \to 0$), and the system reverts to the normal metal phase. At absolute zero, BCS theory predicts that the gap is proportional to the critical temperature, $\Delta(0) \approx 1.764\, k_B T_c$. For aluminum, this superconducting gap corresponds to approximately 50 GHz.

In the next chapter, we will analyze how quasiparticles can couple with the superconducting circuit, resulting in a loss of coherence in transmon qubits. In Chapter 5, the thermal population of quasiparticles will be explained, serving as an argument for the excessive quasiparticle population experimentally observed. We will also discuss the potential mechanisms driving this non-equilibrium population and detail the measures implemented in the shield design to reduce it.

3

Superconducting circuits

In classical information theory, the fundamental unit capable of storing information is the discrete binary state, or bit. By direct analogy, quantum information processing requires an equivalent quantum mechanical unit, the qubit [21]. Consequently, experimental research has focused on identifying physical substrates that allow for the isolation and coherent control of two-level quantum systems.

Superconducting circuits provide a versatile platform for this purpose. By engineering macroscopic microwave circuits cooled to near absolute zero, it is possible to construct *artificial atoms* with tunable energy spectra.

This chapter presents an overview of superconducting circuits, detailing the transmon architecture and its primary decoherence mechanisms. Particular attention is given to quasiparticles, as their dynamics directly motivate the light-tightness measures integrated into the shielding design. Additionally, the interaction between the quantum system and external drive and readout, is described within the context of the dispersive regime and quantum non-demolition (QND) measurements. These principles serve as the theoretical foundation for Chapter 6, which establishes the parameter regimes in frequency and amplitude necessary to shield the circuit against spurious excitations and unwanted state transitions.

3.1 LC circuit as a quantum harmonic oscillator

To understand how a circuit can behave as an atom, we first consider the simplest classical resonant circuit: an LC oscillator composed of a capacitor C and an inductor L. The energy stored in this device can be expressed by the Hamiltonian

$$H = \frac{Q^2}{2C} + \frac{\Phi^2}{2L}, \tag{3.1}$$

where Q is the charge stored on the capacitor and Φ is the magnetic flux in the inductor. Observing the similarities between this Hamiltonian and the one of a mechanical harmonic oscillator with frequency $\omega_r = 1/\sqrt{LC}$, we are prompted to promote the canonical variables to quantum operators $\hat{Q}$ and $\hat{\Phi}$, and impose the commutation relation $[\hat{\Phi}, \hat{Q}] = i\hbar$. We can then define the bosonic annihilation and creation operators as [22]

$$\hat{\Phi} = \sqrt{\frac{\hbar Z_r}{2}}(\hat{a} + \hat{a}^\dagger), \quad \hat{Q} = -i\sqrt{\frac{\hbar}{2Z_r}}(\hat{a} - \hat{a}^\dagger), \tag{3.2}$$

where $Z_r = \sqrt{L/C}$ is the characteristic impedance of the circuit and the prefactors are the zero-point fluctuation of flux Φ_{zpf} and charge Q_{zpf} respectively. Substituting these operators back into the Hamiltonian 3.1 yields the familiar quantum harmonic oscillator (QHO):

$$\hat{H} = \hbar\omega_r \left(\hat{a}^\dagger\hat{a} + \frac{1}{2}\right), \tag{3.3}$$

The eigenstates of this system are the Fock states $|n\rangle$, where the number operator $\hat{a}^\dagger\hat{a} = \hat{n}$ expresses the number of photons inside the resonator.

Because the eigenstates of a harmonic oscillator are equally spaced $E_{ij} = \hbar\omega_r$, any resonant pulse to drive a transition between the ground state $|0\rangle$ and the first excited state $|1\rangle$ will simultaneously drive transitions to higher energy states. Consequently, it is not possible to isolate a two-level subspace.

3.2 Josephson junction-based artificial atoms

The problem of equally spaced energy levels can be solved by introducing a non-linear electrical element into the circuit. In superconducting architectures, this non-linearity is often provided by the Josephson junction. As discussed in Section 2.2.2, JJ consists of two superconductors separated by an oxide barrier. This component allows a dissipationless supercurrent $I = I_c \sin(\varphi)$ to flow across the barrier, where I_c is the critical current and φ is the superconducting phase difference. Because the phase is directly related to the magnetic flux by $\varphi = 2\pi\Phi/\Phi_0$ (with $\Phi_0 = h/2e$ the magnetic flux quantum), the junction acts effectively as a non-linear inductor.

By employing this non-linearity, we can construct a circuit composed by a Josephson junction in parallel with a capacitor C. The Hamiltonian of this system becomes:

$$\hat{H} = 4E_C(\hat{n} - n_g)^2 - E_J \cos(\hat{\varphi}). \tag{3.4}$$

Here, we have introduced the charge number operator $\hat{n} = \hat{Q}/2e$, which encodes the number of Cooper pairs transferred across the junction, and the conjugate phase operator $\hat{\varphi} = 2\pi\hat{\Phi}/\Phi_0$, satisfying the commutation relation $[\hat{\varphi}, \hat{n}] = i$. The quantity $E_C = e^2/2C_\Sigma$ represents the charging energy associated with the total capacitance C_Σ, while $E_J = I_c\Phi_0/2\pi$ is the Josephson energy. Additionally, because the circuit is coupled to a noisy electrostatic environment or external gate voltage, we include a dimensionless parameter n_g to represent the effective offset charge.

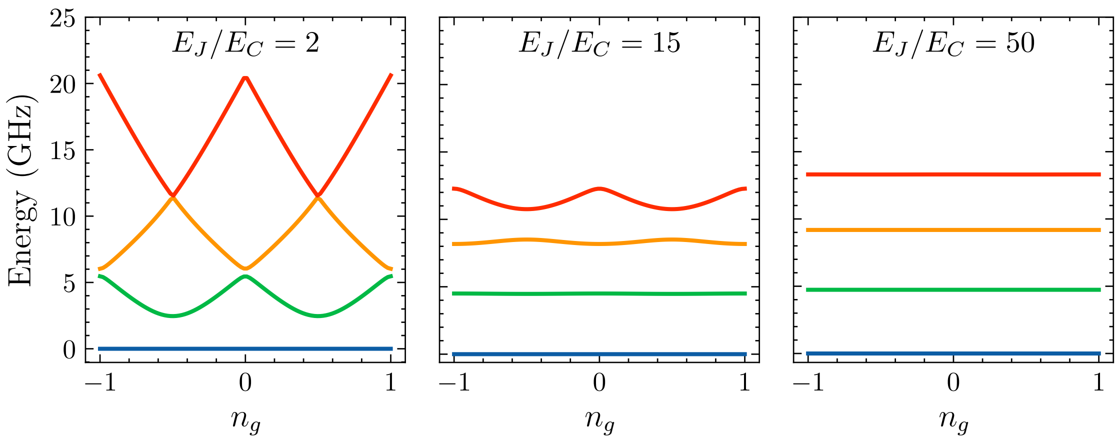

Figure 3.1: Energy difference $\omega_i - \omega_0$ for the spectrum of the Hamiltonian 3.4 as the charge offset n_g and the E_J/E_C ratio changes.

As illustrated in Figure 3.1, the behavior of the circuit depends drastically on the ratio E_J/E_C. In early designs, known as the Cooper-pair box [23], this ratio was kept small $E_J/E_C \lesssim 1$. In this regime, the energy difference between the ground and first excited states depends strongly on the offset charge n_g. While this allows the qubit to be driven efficiently, it also leaves it vulnerable to dephasing due to charge noise. To mitigate this, the transmon qubit was developed [24]. By adding a large parallel capacitor to increase the ratio to $E_J/E_C \gtrsim 50$, the transmon operates in a regime where the charge dispersion is exponentially suppressed. This provides robust immunity to low-frequency charge noise while only sacrificing the anharmonicity algebraically.

In the transmon regime, the variance of the phase fluctuations $\hat{\varphi}$ is small. Therefore, we can expand the cosine term in Equation 3.4 as a Taylor series. By considering only the first two non-vanishing terms and applying the rotating wave approximation (RWA), we obtain the following Hamiltonian:

$$\hat{H} = \hbar\omega_q \hat{b}^\dagger \hat{b} - \frac{1}{2} E_C \hat{b}^\dagger \hat{b}^\dagger \hat{b} \hat{b} \tag{3.5}$$

where $\hbar\omega_q = \sqrt{8E_C E_J} - E_C$ is the qubit transition frequency. In the same fashion as the LC circuit quantization, we have introduced the bosonic annihilation and creation operators $\hat{b}$ and $\hat{b}^\dagger$ through the relations:

$$\hat{\varphi} = \left(\frac{2E_C}{E_J}\right)^{1/4} (\hat{b} + \hat{b}^\dagger), \quad \hat{n} = \frac{i}{2}\left(\frac{E_J}{2E_C}\right)^{1/4} (\hat{b}^\dagger - \hat{b}). \tag{3.6}$$

As discussed previously, adding the non-linearity breaks the degeneracy of the energy levels, and the resulting anharmonic oscillator is characterized by an anharmonicity of approximately $-E_C$. Because of this anharmonicity, we can effectively restrict the system dynamics to the two-level subspace. In this subspace, the ladder operators map to the Pauli matrices, $\hat{b}^\dagger \mapsto |1\rangle\langle 0| = \hat{\sigma}_+$ and $\hat{b} \mapsto |0\rangle\langle 1| = \hat{\sigma}_-$, allowing the Hamiltonian to be written as $\hat{H} = \hbar\omega_q \hat{\sigma}_z/2$.

3.3 Dispersive regime

Having established the fundamental components of superconducting circuits, we now consider their interaction. The simplest interaction between a transmon qubit and a readout resonator is realized via capacitive coupling. In this configuration, the resonator zero-point voltage fluctuations couple directly to the dipole moment of the transmon. This system is well-described by the Jaynes-Cummings Hamiltonian [22]:

$$\hat{H} = \frac{1}{2}\hbar\omega_q \hat{\sigma}_z + \hbar\omega_r \hat{a}^\dagger \hat{a} + \hbar g(\hat{a}^\dagger \hat{\sigma}_- + \hat{a}\hat{\sigma}_+) \tag{3.7}$$

This Hamiltonian couples the degrees of freedom of the transmon and the resonator, mediating the coherent exchange of excitations between the qubit and the cavity field.

For qubit readout, it is advantageous to operate in the dispersive regime, where the detuning $\Delta = \omega_q - \omega_r$ between the qubit and resonator frequencies is large. In this far-detuned limit, the effective coupling strength is weak ($|g/\Delta| \ll 1$), allowing Equation 3.7 to be perturbatively expanded to second order in g/Δ. This yields the effective dispersive Hamiltonian:

$$\hat{H}_{\text{disp}} \approx \frac{1}{2}\hbar\omega_q'\hat{\sigma}_z + \hbar\omega_r'\hat{a}^\dagger\hat{a} + \hbar\chi\hat{a}^\dagger\hat{a}\hat{\sigma}_z \tag{3.8}$$

In this frame, the primary effect of the interaction is to weakly dress the bare frequencies (yielding ω_q' and ω_r') and to introduce a state-dependent dispersive shift parameterized by χ. By factoring the Hamiltonian, it becomes evident that the effective resonator frequency is shifted by $\pm\chi$ depending on the qubit state, forming the fundamental basis for dispersive readout.

Additionally, because the dispersive Hamiltonian commutes with the qubit observable $\hat{\sigma}_z$, the measurement process does not induce transitions between the qubit eigenstates. This allows the measurement to be repeated multiple times without disturbing the post-measurement projected state, a paradigm known as quantum non-demolition (QND) measurement.

In practice, the validity of the dispersive approximation depends not only on the detuning but also on the cavity photon population. The perturbative expansion breaks down if the average number of photons $\bar{n}$ approaches the Jaynes-Cummings critical photon number, defined as $n_{\text{crit}} = (\Delta/2g)^2$. Experimentally, probing the cavity with a larger photon number improves the readout signal-to-noise ratio. However, strong readout drives can induce spurious excitations of the qubit [12]. These events, known as measurement-induced state transitions (MIST), degrade readout fidelity and are particularly detrimental in sensing applications. The dynamics governing these mechanisms will be analyzed in detail in Chapter 6.

3.4 Decoherence in superconducting qubits

In the experimental implementation of these circuits, uncontrollable factors in the surrounding environment can interact with the qubit, leading to a loss of coherence and a reduction in operational fidelity. These sources of error have become a central focus within the quantum information science community. Not only they are one of the main limitation to scalability in quantum computing, but they are also a crucial limitation in quantum sensing, where dark counts (false positive events) is one of the primary figure of merit.

To quantitatively describe how these environmental interactions degrade quantum information, we describe a two-level system using the Bloch sphere representation. Here, a pure state can be expressed as $|\psi\rangle = \cos(\theta/2)|0\rangle + e^{i\phi}\sin(\theta/2)|1\rangle$, where we map the ground state $|0\rangle$ to the north pole and the excited state $|1\rangle$ to the south [7]. The vertical z-axis defines the longitudinal axis, while the x-y plane forms the transverse direction.

The decay of this quantum state is generally characterized by two distinct rates:

- **Longitudinal relaxation rate ($\Gamma_1 = 1/T_1$):** This rate describes the depolarization of the qubit along the quantization axis. It incorporates the contributions of relaxation from the excited state to the ground state (Γ_{10}) and the reverse process (Γ_{01}), such that $\Gamma_1 = \Gamma_{1\to0} + \Gamma_{0\to1}$. Following the principle of detailed balance under Boltzmann statistics at the millikelvin operational temperatures of a dilution refrigerator, the thermal excitation rate Γ_{01} is exponentially suppressed. Therefore, $\Gamma_1 \approx \Gamma_{10}$, indicating that the qubit predominantly tends to lose energy to the colder environment.

- **Transverse relaxation rate ($\Gamma_2 = 1/T_2$):** This rate is composed of a combination of the longitudinal relaxation limit and the pure dephasing rate, given by $\Gamma_2 = \Gamma_1/2 + \Gamma_\varphi$. Pure dephasing tracks the loss of phase information along the transverse plane. Physically, Γ_2 represents the rate at which a coherent superposition is lost, or equivalently, the decay of the off-diagonal elements in the density matrix $\rho = |\psi\rangle\langle\psi|$ that describes the quantum system.

While superconducting circuits are subject to multiple decoherence mechanisms [7], including flux noise [25] and coupling to two-level systems (TLS) [26], the remainder of this section will focus specifically on quasiparticle tunneling. Understanding this particular decoherence channel is essential, as it provides the primary physical motivation for the light-tightness measures integrated into the shield design presented in Chapter 5.

3.4.1 Quasiparticle tunneling

One of the most prominent decoherence processes affecting Josephson junction-based superconducting circuits is the coupling between the qubit and the quasiparticles that tunnel across the junction [27]. For a Josephson junction comprising a left and a right superconducting electrode separated by an insulating barrier, the total Hamiltonian of the system can be written as:

$$\hat{H} = \hat{H}_{\varphi} + \hat{H}_{\mathrm{QP}} + \hat{H}_{\varphi,\mathrm{QP}}, \tag{3.9}$$

where $\hat{H}_{\varphi}$ is the isolated qubit Hamiltonian and $\hat{H}_{\mathrm{QP}}$ governs the quasiparticle dynamics. Following the formalism introduced in Equation 2.9, $\hat{H}_{\mathrm{QP}} = \sum_{L,\sigma} E_L \hat{\gamma}^{\dagger}_{L\sigma}\hat{\gamma}_{L\sigma} + \sum_{R,\sigma} E_R \hat{\gamma}^{\dagger}_{R\sigma}\hat{\gamma}_{R\sigma}$ accounts for the quasiparticle excitations in both the left (L) and right (R) electrodes. The interaction term $\hat{H}_{\varphi,\mathrm{QP}}$ couples the superconducting phase difference across the junction to the quasiparticle degrees of freedom. This term contains operator products of the form $e^{i\hat{\varphi}/2}\hat{\gamma}^{\dagger}_{L\sigma}\hat{\gamma}_{R\sigma}$ and their Hermitian conjugates. Physically, these terms describe the tunneling mechanism where a quasiparticle is annihilated in one electrode (e.g., $\hat{\gamma}_{R\sigma}$) and created in the opposite electrode (e.g., $\hat{\gamma}^{\dagger}_{L\sigma}$), with a shift in the phase as result. A complete derivation of these tunneling matrix elements is detailed in Reference [28].

Treating this interaction perturbatively, Fermi's golden rule can be employed to compute the corresponding qubit transition rates $\Gamma^{\mathrm{QP}}_{ij}$. We define the normalized quasiparticle fraction as $x_{\mathrm{qp}} = n_{\mathrm{qp}}/n_{\mathrm{cp}}$, where n_{qp} and n_{cp} are the densities of quasiparticles and Cooper pairs, respectively. Under this framework, the tunneling of quasiparticles across the junction drives energy relaxation in the qubit at a rate given by:

$$\Gamma^{\mathrm{QP}}_{10} = \frac{16E_J}{\hbar\pi}\sqrt{\frac{E_C}{8E_J}}\sqrt{\frac{\Delta}{2\hbar\omega_{10}}}\,x_{\mathrm{qp}}. \tag{3.10}$$

Consequently, the presence of quasiparticles constitutes a fundamental limitation for both superconducting qubits and related quantum sensors. Quasiparticle poisoning degrades the performance of these architectures by increasing the energy relaxation rate and generating spurious excited-state populations, which rises the dark count rates in sensing applications. In Chapter 5, we will further analyze the steady-state quasiparticle fraction x_{qp} and its nonequilibrium distribution, providing the physical justification for our engineering efforts to shield the device from stray environmental radiation.

4

Magnetic field shielding

Superconducting quantum circuits are sensitive to stray magnetic fields. An uncontrolled magnetic environment degrades the coherence and performance of both qubits and microwave resonators. Fields exceeding the critical magnetic field of the material (10.5 mT for bulk aluminum, for instance) destroy the superconducting phase, causing the metal to revert to its normal resistive state.

However, background fields well below this critical threshold, such as the Earth's magnetic field, also remain detrimental. While bulk Type I superconductors exhibit perfect diamagnetism, thin films behave as Type II superconductors [29] instead. Consequently, when a thin film is cooled below its transition temperature in a residual out-of-plane magnetic field, the magnetic flux is not entirely expelled. Instead, it penetrates the film and becomes pinned as quantized, Abrikosov vortices. Under applied microwave excitation, the motion of trapped vortices leads to energy dissipation [30].

In addition, weak magnetic fluctuations couple directly to the circuits. Many architectures, such as the flux tunable transmon and resonator, employ Superconducting Quantum Interference Device (SQUID) loops to control their transition frequencies via an external magnetic flux. Consequently, any variation in the ambient field shifts the component frequencies, making the system susceptible to frequency jitter.

To protect the quantum states against these mechanisms, the experimental setup must be magnetically shielded. The standard requirement is to attenuate the ambient magnetic field to a level where less than a single magnetic flux quantum ($\Phi_0 = h/2e \approx 2.07 \times 10^{-15}$ Wb) penetrates the active area of the device. For a typical circuit footprint of approximately $100 \times 100\ \mu\text{m}^2$, this requires suppressing the background field to below 200 nT.

The efficacy of a magnetic shield is quantitatively evaluated using the shielding factor, S. This figure of merit characterizes the attenuation of the external magnetic field B_0 to the residual interior field B_{int}, and can be expressed either as a linear ratio or on a logarithmic scale:

$$S = \frac{B_0}{B_{\text{int}}}, \qquad S_{\text{dB}} = 20 \log_{10} \left(\frac{B_0}{B_{\text{int}}} \right). \tag{4.1}$$

As discussed in the introduction, the deployment of quantum sensing devices in experimental setups frequently subjects them to high field environments. For instance, electron spin spectroscopy operate in ambient magnetic fields that can reach 500 mT [2]. Similarly, fundamental physics experiments searching for dark matter axions employ haloscopes that employ magnetic fields reaching 10 T [6]. Although active compensation coils are used, spatial field maps reveal that the residual magnetic flux density at the location of the superconducting circuit can still reach values up to 80 mT. To establish a robust operational margin, the shield design presented in this chapter is specifically engineered to attenuate external fields up to 100 mT. To reliably suppress a background field of this magnitude down to sub-flux-quantum regime, the shielding architecture must achieve a total attenuation factor between 10^5 and 10^6.

4.1 Shunting magnetic fields with ferromagnetic materials

While the Meissner effect allows superconductors to completely expel weak magnetic fields, they must be operated well below their critical field B_c. Normal ferromagnetic materials are therefore employed as a primary shielding layer to pre-attenuate the ambient environment. Furthermore, because background fields such as the Earth's magnetic field ($\sim 50\ \mu$T) can be trapped during the initial cryostat cooldown, the shielding architecture must be functional even at room temperature. In this section, we analyze the fundamental principles of magnetic shunting using ferromagnetic materials. We establish the analytical framework for modeling field attenuation and discuss the selection of our material stack based on key quantities such as magnetic permeability and field saturation.

4.1.1 Analytical results for infinite cylinders

If we consider a infinite cylinder with inner radius a of a materials with permeability μ_r subjected to an external field B_0, it is possible to compute analytically the value of the field inside by employing the magnetic scalar potential ψ and ensuring its continuity in the boundaries. In the limit of high permeability $\mu_r \gg 1$ and small thickness $t \ll a$, then we can find the shield factor to be:

$$S = \frac{\mu_r t}{2a} \tag{4.2}$$

The full derivation can be found in Appendix A. In the same way, we can compute the attenuation of multiple shield by concatenating the different boundary conditions. If we consider two shields with respectively shielding factor S_1 and S_2 and internal radius a_1 and a_2 we find:

$$S_{\text{tot}} = S_1 S_2 \left(1 - \frac{a_1^2}{a_2^2}\right) + S_1 + S_2 \tag{4.3}$$

Is important to notice that the multiplicative effect of the shielding factor is stronger when the layers are far apart (i.e. $a_1 \ll a_2$). Again, the full derivation for an arbitrary stack of layers can be found in Appendix A.

By checking with numerical values for materials with high permeability as Mu-metals with $\mu_r \sim 10^5$ and thickness in the order $t \sim 10^{-3}$ m and radius $a \sim 10^{-2}$ m we obtain shielding factors on the order of 10^4. Therefore, combining a pair of Mu-metal shield should give already the desiderate attenuation. This however is not the case. Because of the saturation of the magnetic domains inside the ferromagnetic materials, the permeability is strongly dependent on the magnetic field with a non-linear relation known as B-H curve, at a point that in high enough field, the differential permeability decreases toward the vacuum levels μ_0.

4.1.2 Field saturation

Because of the non-linear relation between the magnetic flux density B and the applied field H, we need to consider not only the maximum value of the permeability μ_r^{max}, but also its saturation B_{sat}. In Figure 4.1 the permeability of materials considered in the shield design are showed as the external field is changed. Nickel-iron based alloys as Mu-metal can reach very high values of permeability $\sim 70\,000$, however its critical field is relatively low ~ 0.7 T, therefore the approach used to define the layers stack for the shield uses a graded permeability approach: outer layers uses high-saturation materials (as pure iron or low-carbon steel) to absorb the bulk flux, leaving lower field inside the low-saturation but high permeability mu-metal shield.

It is important to notice that different compositions and annealing process can exhibit significantly different magnetic properties. The data reported is the one used in the results of Section 4.3.2 as they comes from the build-in COMSOL material library.

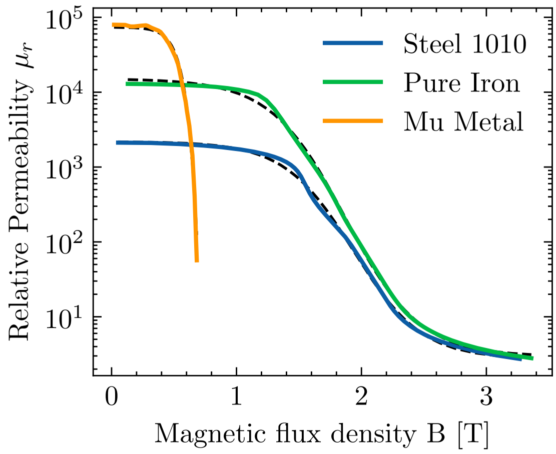

Material	B_{sat} (T)	$\mu_r^{\max}$
Mu-metal	0.7	70 000
Steel 1010	1.8	2 000
Pure iron	1.9	15 000

Figure 4.1: The relative permeability (μ_r) of various ferromagnetic materials. The dashed black line represents a curve $\mu_r(B) = (\mu_r^{\max} - d)/(1 + e^{b(x - B_{\text{sat}})}) + d$ that was fitted numerically to determine the maximum permeability $\mu_r^{\max}$ and the saturation field B_{sat}. The data used in this analysis was provided by COMSOL Multiphysics.

4.1.3 Cryogenic considerations

Both magnetic permeability and saturation flux density are significantly affected by cryogenic temperatures. Ferromagnetic materials naturally contain microscopic inclusions and residual internal microstresses [31]. At low temperatures, the thermal activation energy required for magnetic domain walls to overcome these physical defects is drastically reduced. Consequently, these inclusions and stress points act as pinning sites that decrease domain wall motion. This results in a measurable reduction in maximum magnetic permeability, alongside a slight increase in the saturation flux density.

This behavior is highly material-specific and strongly dependent on prior thermal and mechanical treatments. Literature indicates that cooling steel alloys to liquid nitrogen (LN) temperatures results in an approximate 8% decrease in maximum permeability and a 4% increase in saturation flux density [32]. It should be noted, however, that these specific tests were conducted at 77 K and on different steel grades than the AISI 1010 analyzed in this report. Further studies confirm this general trend, demonstrating a slight decrease in the maximum permeability of ARMCO pure iron at liquid helium (LHe) temperatures [33].

In contrast to pure iron and low-carbon steels, high-permeability nickel-iron alloys like standard Mu-metal suffer a more drastic performance drop. To operate effectively in cryogenic settings, these alloys require specialized hydrogen annealing to reduce inclusions and optimize their magnetic parameters for cryogenic temperatures. This cryogenically optimized family of alloys is commercially known as Cryoperm. Given its high permeability at low temperature, Cryoperm has been selected for the innermost ferromagnetic layer of the shield.

4.2 Expelling magnetic field with superconductors

While ferromagnetic materials provide substantial magnetic field attenuation, relying exclusively on them to reach the desired shielding targets would require multiple thick layers to prevent the magnetic saturation discussed in Section 4.1.2. Given the strict spatial constraints of a typical dilution refrigerator, along with the extended cooldown times associated with large thermal masses, constructing a compact shield solely from ferromagnets is impractical. By leveraging the complete flux expulsion of Type I superconductors via the Meissner effect, alongside the enhanced field resilience of Type II superconductors, hybrid designs can achieve high attenuation within a limited volume [34, 35]. In this section, we analyze the capabilities and physical limitations of employing superconducting layers for magnetic shielding.

4.2.1 Type I superconductors and perfect diamagnetism

Based on the analysis in Section 2.1 regarding the exponential decay of the magnetic flux density at a superconducting boundary, macroscopic layers composed of Type I superconductors can be treated as perfect diamagnets. Under this approximation, it is possible to analytically derive the magnetic field attenuation for a superconducting cylindrical cup of inner radius a and height L. As one moves along the cylinder z-axis, the shielding factor takes the form:

$$S(z) \approx e^{\alpha_1 z/a}, \tag{4.4}$$

where $\alpha_1 \approx 2.405$ is the first root of the zero*th*-order Bessel function of the first kind. A complete derivation of the exact shielding factor is provided in Appendix A.

4.2.2 Type II superconductors and mixed phase

Simulating Type II superconductors presents significant challenges, primarily due to the computational cost of modeling the microscopic behavior of Abrikosov vortices. While it is theoretically possible to solve numerically the time-dependent Ginzburg-Landau equations using finite element methods [36], the vast length-scale disparity between individual flux vortices $\mathcal{O}(1\,\mu\text{m})$ and the macroscopic shield dimensions necessitates a huge number of mesh elements, resulting in computational intractability. To overcome this, several macroscopic models of superconductivity have been proposed. This section discusses the Critical State Model (CSM), which provides both a practical simulation methodology and a robust framework for deriving analytical shielding requirements.

Critical state model and E-J power law

Instead of explicitly tracking the dynamics of flux vortices, we can macroscopically describe their behavior using a non-linear material resistivity [37]. According to these models, thermally activated flux creep generates an electric field

$$\mathbf{E}(\mathbf{J}) = E_c \frac{\mathbf{J}}{|\mathbf{J}|} \exp\left[\frac{U_0}{k_B T}\left(\frac{|\mathbf{J}|}{J_c} - 1\right)\right] \tag{4.5}$$

where U_0 is the activation energy of the vortex bundle and J_c is the critical current density that causes an electric field E_c (typically defined arbitrarily, often as 10^{-4} V/m). This relationship is frequently simplified to a power law:

$$\mathbf{E}(\mathbf{J}) = E_c \frac{\mathbf{J}}{|\mathbf{J}|} \left(\frac{|\mathbf{J}|}{J_c}\right)^n \tag{4.6}$$

where $n = U_0/k_B T$. For low temperature and *hard* superconductors, $n \gg 1$. In this limit, the E-J power law transitions into the Critical State Model (CSM), which postulates that: *any non-zero macroscopic electric field induces a current density exactly equal to J_c.*

Analytical results for type II SC infinite cylinders

Consider a infinitely long cylinder of inner radius a ant thickness t, constructed from a Type II superconductor. Assume a uniform transverse magnetic field B_0 is applied. If $B_{c1} < B_0 < B_{c2}$, the material enters the mixed state, allowing magnetic flux to penetrate via vortices. Under the CSM, this vortex penetration is macroscopically represented by a screening current of density J_c that begins flowing at the outer surface to cancel the incident field B_0.

For analytical tractability, we assume the axial screening current $\pm J_c\hat{\mathbf{z}}$ flows in the region bounded by the outer surface of the cylinder and an internal ellipsoidal penetration front [38], which can be parameterized in polar coordinates by:

$$u(\theta, \xi) = x^2 + y^2 = \frac{a\xi}{\sqrt{1-(1-\xi^{2-2/n})\sin^2\theta}} \tag{4.7}$$

where $a\xi$ dictates the position of the penetration front along the principal axis, and n defines the ellipticity. As the external field B_0 increases, a greater total screening current is required. Because the CSM restricts the local current density to J_c, the superconductor responds by expanding the depth of the current-carrying region, driving the penetration front ξ deeper towards the center (see Figure 4.2). If the penetration depth exceeds the wall thickness $a(1-\xi) > t$, the shield reaches its saturation and the magnetic flux leaks into the shielded volume.

To determine the minimum thickness required for a Type II superconducting cylinder to maintain a zero-field interior, we apply the Biot-Savart law to compute the field generated by the current distribution bounded by this ellipsoidal shell:

$$\boldsymbol{B}(\boldsymbol{r}) = \frac{\mu_0 I}{4\pi}\oint \frac{d\boldsymbol{r}\times(\boldsymbol{r}-\boldsymbol{r}')}{|\boldsymbol{r}-\boldsymbol{r}'|^3} = \frac{\mu_0 I}{2\pi r}\hat{\boldsymbol{e}}_\theta \tag{4.8}$$

We integrate the current density J_c over the cross-section to find the effective screening field. By symmetry, we evaluate only the contribution from the $+J_c$ region on the positive x-axis:

$$B_\theta(\xi) = 2\frac{\mu_0}{2\pi}\int_{-\pi/2}^{\pi/2} d\theta \int_{u(\theta)}^{a} \frac{J_c r\cos\theta}{r}\, dr d\theta = \frac{2\mu_0 J_c a}{\pi}\left(1-\xi\frac{\arcsin\sqrt{1-\xi^{2-2/n}}}{\sqrt{1-\xi^{2-2/n}}}\right)$$

The bracketed term depends weakly on n and can be approximated as $1-\xi$. To successfully shield the interior, the magnetic field generated by these supercurrents must exactly cancel the external field, meaning $B_\theta(\xi) = B_0$. Inverting this relationship yields the position of the current front. To ensure zero field inside the hollow cylinder, the penetration front must not reach the inner wall, requiring $1 - \xi < t/a$.

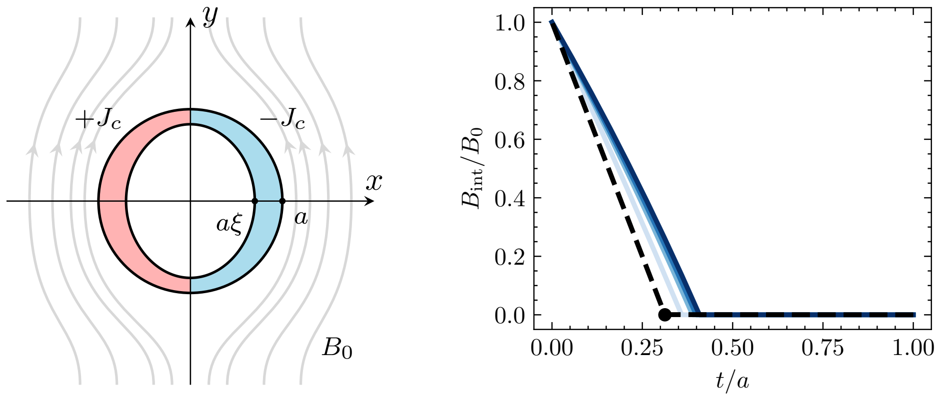

Figure 4.2: (Left) Schematic representation of the $\pm J_c$ current density ellipsoid profile flowing along the z-direction. (Right) Magnetic field intensity inside an infinite type II superconducting cylinder as a function of the wall thickness t for varying ellipticity n (blue shading indicates values from 2 to 100), compared with the linear approximation (black dashed line). When the thickness exceeds the critical threshold defined by Equation 4.9 (black dot), the external magnetic field B_0 is completely shielded. The plot is generated for a cylinder of radius $a = 40$ mm with a critical current density $J_c = 10^9$ A/m^2 and an applied field $B_0 = 10$ T.

This condition yields the minimum thickness required for an infinitely long Type II superconducting cylinder to effectively shield its interior, mimicking a Meissner state:

$$t > \frac{\pi B_0}{2\mu_0 J_c} = 0.125\ \mathrm{mm} \left(\frac{B_0}{100\ \mathrm{mT}}\right) \left(\frac{10^9\ \mathrm{A/m^2}}{J_c}\right) \tag{4.9}$$

Despite the lack of a precise literature reference for the critical current density J_c of the specific Type-II superconductor (a lead-tin alloy) used in the final design, typical values for critical current densities generally range from 10^8 to 10^{11} A/m^2. Therefore, this analytical model demonstrates that a Type-II superconducting layer with a thickness on the order of 1 mm is sufficient to guarantee perfect internal shielding even within the mixed phase. In this regime, the material functions equivalently to the Type-I Meissner mechanism discussed in the previous section.

4.3 Shield design and simulations

Subject to the spatial constraints imposed by the physical dimensions of the sample holder and the clearance required for the SMA feedthrough connectors, the internal diameter of the shield is set to 80 mm. According to the analytical approximation in Equation 4.4, achieving a transverse magnetic attenuation factor of 10^5 with this diameter would necessitate a shield height of approximately 190 mm. However, as the magnetic field approaches the completely diamagnetic bottom enclosure, it is forced to zero. By applying the more exact analytical treatment from Equation A.12, a shorter cylindrical profile is allowed. Furthermore, capping the assembly with a superconducting lid provides supplementary attenuation. This configuration allows the total height of the shield to be reduced to less than 150 mm. This initial analytical intuition is subsequently corroborated through the numerical simulations presented in the following sections.

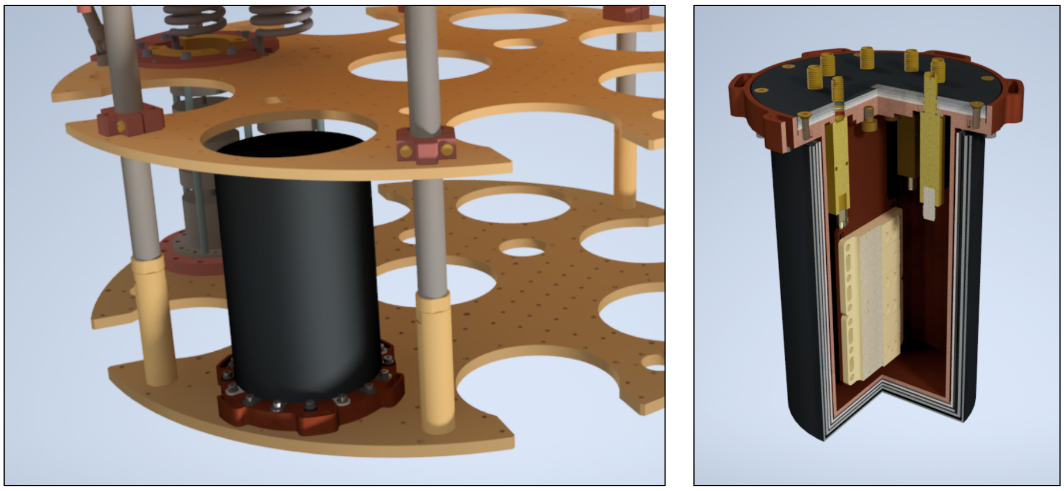

Figure 4.3: 3D rendering of a (right) quarter-section cutaway of the magnetic shield and its physical positioning inside a Bluefors XLD dilution refrigerator (left).

The material selection for the shielding stack reflects the graded permeability and superconducting principles established in the previous sections. The outermost layer is constructed from 1010 Steel, a ferromagnetic material with high field saturation and good magnetic permeability. Progressing inward, the intermediate layer consists of a Type II superconducting Lead-Tin alloy (60% Sn, 40% Pb). Even in a deeply saturated state of the Steel, the upper critical field of 155 mT [39], ensure perfect diamagnetic screening at a thickness of $\sim$ 1 mm, as analyzed in

Section 4.2.2. Any residual magnetic flux that either penetrates the bulk or leaks through the gap between the cylindrical layers and the lid, is subsequently attenuated by an inner Cryoperm shell. Because the outer layers have already substantially reduced the ambient field, the Cryoperm layer operates well below its saturation threshold, providing an attenuation factor of up to 10^4. This attenuation ensures that the innermost layer, a Type I superconducting aluminum shell, operates safely within its strict Meissner phase.

In addiction, this specific configuration ensures effective magnetic shielding even at room temperature, thereby mitigating the risk of flux trapping during the cryostat cooldown. This operational advantage, along with the electromagnetic characteristics of this design, will be evaluated in the following sections through a comprehensive suite of numerical simulations aimed at validating the shield's overall performance.

The complete mechanical specifications and drawings of the shield assembly are provided in Appendix B along with thermal consideration. The detailed design of the lid structure is instead presented in Chapter 5, as its geometry is chosen to provide light-tightness.

4.3.1 Zero-field cooldown

The operational protocol for the device begins with a zero-field cooldown to prevent initial magnetic flux trapping. During the initial cooling phase from room temperature, the superconducting layers remain inactive. Consequently, the system relies entirely on the ferromagnetic layers, specifically the steel and Cryoperm shells, to shunt the ambient Earth's magnetic field. The use of a Cryoperm shield is highly effective in this regime, as it has been shown to attenuate room-temperature magnetic fields by a factor of approximately 1000. This pre-attenuation ensures that as the device transitions through its critical temperature T_c, the local magnetic flux density at the surfaces of the superconducting shells is heavily suppressed. Numerical simulations validating this room-temperature operation will be detailed in the subsequent section.

Once the system reaches its base temperature and the superconducting layers become fully active, the external magnetic field is slowly ramped to the target operational level. Provided the field remains below B_c, the superconducting shells will completely expel the applied magnetic flux. However, the ramp rate of the external magnet must be carefully controlled. A rapidly changing magnetic field can induce excessive eddy currents within the ferromagnetic layers, leading to unwanted thermal power dissipation. A simulation of these transient dynamics will be presented to establish a safe magnetic field ramp rate.

4.3.2 Introduction to finite element methods

The finite element method (FEM) is a computational technique used to numerically solve partial differential equations by subdividing the continuous spatial domain Ω into discretized elements known as a mesh [40]. Each mesh element, typically triangles in two dimensions and tetrahedra in three dimensions, is used to decompose the unknown solution u into a linear combination of polynomial basis functions ϕ_i, also called trial functions:

$$u = \sum_{i=1}^{N} c_i \phi_i, \tag{4.10}$$

where the coefficients c_i represent the degrees of freedom to be determined by the solver.

If the solution is a scalar field, standard Lagrange (or nodal) finite elements are generally employed. In this approach, the degrees of freedom correspond to the values at the vertices of the mesh, and the basis functions interpolate these nodal values. Therefore, Lagrange elements enforce continuity across the boundaries of all adjacent elements. However, this causes the method to fail when applied to vector fields with a non-zero curl, such as magnetic fields. To resolve this, Nédélec (or edge) elements are utilized. For Nédélec elements, the degrees of freedom are associated with the edges (or faces in 3D) of the mesh rather than the nodes. This functional space space guarantee continuity of the tangential components across element boundaries while allowing discontinuities in the normal components.

The H-formulation

To model the electromagnetic response of the system, we consider Faraday's law of induction, $\nabla \times \mathbf{E} = -\partial_t \mathbf{B}$, and Ampère's law. Under the magneto-quasistatic approximation, the displacement current $\partial_t \mathbf{D}$ is negligible, reducing Ampère's law to $\nabla \times \mathbf{H} = \mathbf{J}$. Using Ohm's law, $\mathbf{E} = \rho \mathbf{J}$, we can combine these relations to derive the H-formulation [41] of Maxwell's equations:

$$\nabla \times (\rho \nabla \times \mathbf{H}) = -\frac{\partial \mathbf{B}}{\partial t}. \tag{4.11}$$

In this formulation, the magnetic flux density is given by $\mathbf{B} = \mu(\mathbf{H})\mathbf{H}$, where the permeability $\mu(\mathbf{H})$ accounts for the non-linear B-H relations of the materials. Additionally, the resistivity ρ can depend on the current density, as demonstrated by the E-J power law discussed in Section 4.2.2, yielding a state-dependent resistivity $\rho(\mathbf{J}) = \rho(\nabla \times \mathbf{H})$.

Variational formulation for non-linear problems

To solve Equation 4.11 using FEM, the partial differential equation must be recast into its weak, or variational, form [40]. This is achieved by taking the inner product of the equation with a vector test function $\mathbf{v}$ and integrating over the entire spatial domain Ω. Applying integration by parts and enforcing appropriate Dirichlet boundary conditions, the surface integral terms vanish. The resulting variational formulation requires finding an $\mathbf{H}$ such that:

$$\int_\Omega \frac{\partial \mathbf{B}}{\partial t} \cdot \mathbf{v} \, d\Omega + \int_\Omega \rho(\nabla \times \mathbf{H}) \cdot (\nabla \times \mathbf{v}) \, d\Omega = 0 \tag{4.12}$$

holds for all valid test functions $\mathbf{v}$. This integral equation forms a system of non-linear algebraic equations, $F(\mathbf{H}, \mathbf{v}) = 0$. The system is typically solved iteratively using a Newton-Raphson algorithm to determine the coefficients c_i from Equation 4.10 in the Nédélec edge element basis.

4.3.3 Numerical results

During the preliminary phase of the simulation framework development, several numerical solvers were evaluated. The initial studies were conducted using FEMM (Finite Element Method Magnetics) [42], an open-source 2D solver. While FEMM allows for the rapid simulation of non-linear B-H curves of ferromagnetic materials, it lacks the capability to incorporate the non-linear resistivity required to model Type II superconductors. A second open-source alternative, FEniCSx [43], was also explored. FEniCSx offers an exceptional degree of flexibility, allowing users to define arbitrary partial differential equations directly in their weak variational form. However, while this high level of control is ideal for simulating a broad class of models, even beyond CSM, the reliance on external meshing tools and a highly involved software framework made it impractical for rapid prototyping. Consequently, the commercial finite element software COMSOL Multiphysics was selected as the primary simulation environment. This software natively supports the H-formulation, allowing the explicit definition of both custom non-linear resistivity models and B-H curves within a unified interface.

It is important to note that simultaneously simulating the full E-J power law for superconductors alongside ferromagnetic non-linearities is computationally expensive, primarily due to two factors. First, the shield's geometry comprises very thin walls; the resulting high aspect ratio of the mesh elements degrades matrix conditioning and undermine solver convergence. Second, the formulation itself is computationally demanding: capturing the dynamics of Type II superconductors requires a time-dependent transient simulation to correctly model the induced critical current J_c. Furthermore, the H-formulation relies on Nédélec edge elements to accurately represent the vector field, which consume more memory and give rise to higher computational cost compared to standard Lagrange nodal elements.

To mitigate these computational costs, appropriate physical approximations must be applied when valid. If a Type II superconducting layer can be safely approximated as a perfect diamagnet (either because it remains strictly within the Meissner phase or possesses sufficient thickness to fully screen the field, as established in Section 4.2), it is more efficient to omit the H-formulation and use instead the standard magnetic vector potential (A-formulation) within a purely magnetostatic solver.

Validation of Type II superconductor behavior

As explained in the previous section, the simulation of a Type II superconductor can be implemented using the E-J power law. Within COMSOL Multiphysics, the *Magnetic Field Formulation* (H-formulation) allows to specify a custom, non-linear relationship for the electric field E. The remaining materials in the shield can be simulated using the simpler A-formulation (*Magnetic Fields* interface), which natively handles non-linear materials with custom B-H curves. The multiphysics coupling between these domains is achieved by enforcing electric and magnetic field continuity at the boundaries separating the two physics formulations.

A primary issue with explicit Type II simulations is the high computational cost and the instability of the solver convergence. Accurately capturing the steep spatial change of the critical current density J_c requires an extremely fine mesh. In Figure 4.4, 20 radial mesh elements were utilized across the superconducting layer; even with this high mesh density, numerical artifacts remain visible at the current penetration front. Despite this, the analytical solution for the front position, derived using the Critical State Model (CSM), demonstrates good agreement with the numerical simulation. The most prominent discrepancy is the smooth spatial decay of the simulated current density, as opposed to the sharp step-function change from J_c to zero predicted by the CSM. The reason of this smoothing can be found on the finite exponent n (set to 80 in the present simulation); increasing n asymptotically recovers the strict CSM limit.

The overhead of the H-formulation and the necessity of running a time-dependent solver (in Figure 4.4, a linear field ramp to 150 mT was applied) increase further the computational load.

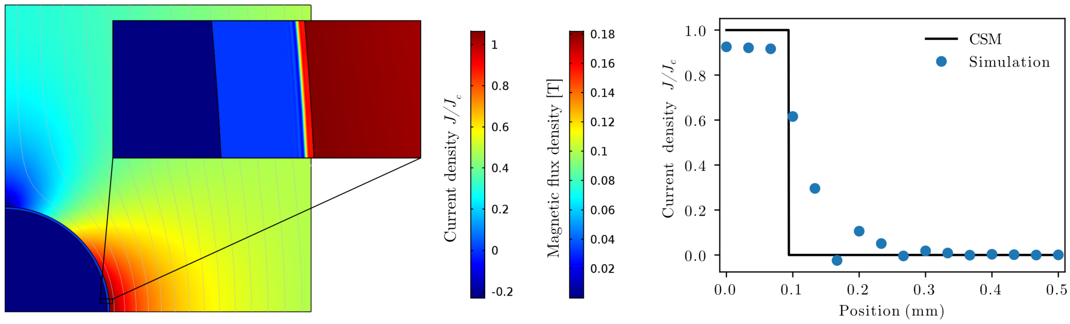

Figure 4.4: COMSOL Multiphysics simulation of a Type II superconducting shell characterized by a critical current density $J_c = 2 \times 10^9$ A/m^2 and an E-J power law exponent $n = 80$. A uniform external transverse magnetic field of $B_0 = 150$ mT is applied along the y-axis. (Left) Two-dimensional cross-section illustrating the magnetic flux density norm alongside the induced axial screening current density, J/J_c, within the superconducting layer. (Right) Radial profile of the normalized current density, J/J_c, measured inward from the outer radius ($a = 40$ mm), plotted in comparison with the analytical predictions of the CSM.

Nevertheless, as predicted by the analytical formalism, the magnetic field inside the bulk of the Type II superconductor is essentially zero. This observation justifies a major physical simplification, rendering full 3D simulations tractable. By treating the macroscopic behavior of the Type II superconductor identically to a Type I material (provided the applied field satisfies $B < B_{c2}$), we can model it as a perfect diamagnet.

Lid field dynamics

The primary failure mode of the shield design arises from the risk of exceeding the critical magnetic field of the superconducting layers. Furthermore, even when the external field remains safely below this critical threshold and the superconductors operate strictly within their Meissner (or mixed) states, magnetic flux penetrating the physical gap between layers and lid degrades the overall field attenuation (see Equation 4.4). To analyze the local magnetic field dynamics in the vicinity of the lid, a 2D simulation was conducted.

Figure 4.5 illustrates the cross-sectional field profile at the conjunction between the lid and the cylindrical walls. Moving from the innermost layer outward, the shielding stack comprises a Type I superconductor (e.g., aluminum), a Cryoperm layer, a Type II superconductor (e.g., Niobium or a Lead-Tin alloy), and an outermost layer of 1010 Steel. Incident magnetic field lines attempting to penetrate the shielded volume are effectively collected by the outermost steel layer and shunted around it. The two colormaps display the magnetic flux density norm for all domains, except for the Type II superconductor (the second outermost layer), where the normalized current density is represented.

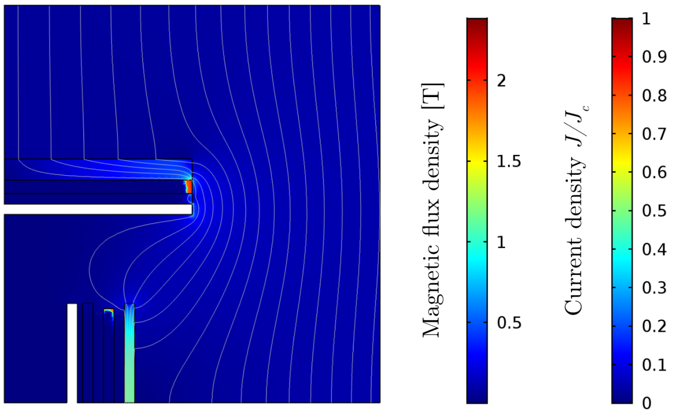

Figure 4.5: Profile simulation of the shield is presented. The type I superconductor is assumed to be a perfect diamagnet, while the Type II superconductor employs the E-J power law. The second color bar represents the ratio J/J_c flowing through the material, relative to the Type II superconductor. The first color bar shows the magnetic flux density in Tesla, relative to the rest of the domain. The simulation was performed using COMSOL Multiphysics with an external magnetic field $B_0 = 100$ mT and with $J_c = 10^9$ A/m^2.

A potential source of concern is the relatively high field concentration observed in proximity to the superconducting layers. This effect is visible in the redd regions of the Type II superconductor, where a critical current J_c front expands to cancel the external field. However, because the experimental protocol requires operation under a static DC external field, pinned flux vortices will not contribute significantly to dissipation. If the shield were instead required to operate in time-varying external fields, a more complex architecture might be necessary, such as physically recessing the superconducting layers and extending the ferromagnetic layers to act as active flux diverters [44].

Axial and transverse field

Following preliminary validations of the Type II superconductor behavior, we proceed to analyze the complete shield geometry. The most efficient approach for this initial analysis is a 2D axisymmetric simulation. This method exploits the rotational symmetry of the system; however, it limits the orientation of the applied magnetic field. To satisfy the divergence-free condition imposed by Maxwell's equations, the external field must be oriented parallel to the axis. Despite this limitation, the 2D axisymmetric approach, combined with the perfect diamagnet approximation for the Type II superconducting layers, yields a computationally inexpensive simulation that converges on the order of tens of seconds.

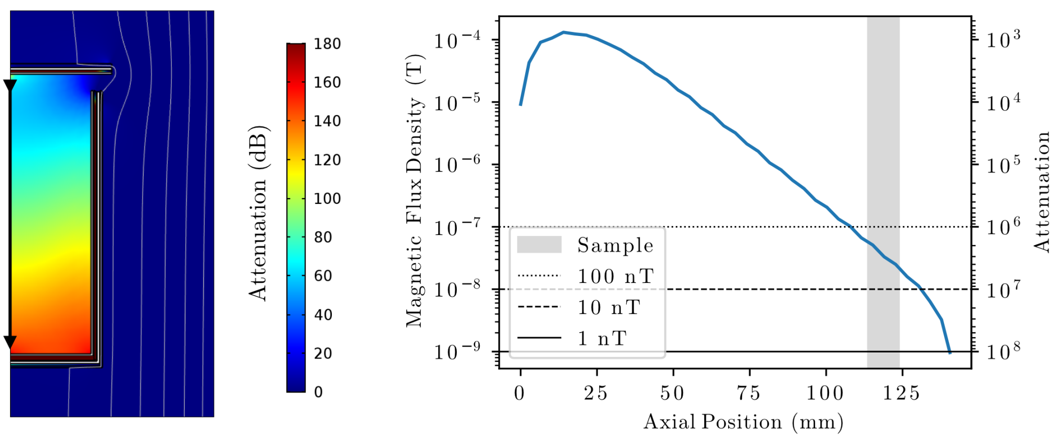

Figure 4.6: 2D axisymmetric magnetostatic simulation performed using COMSOL Multiphysics. A uniform external field of $B_0 = 100$ mT is applied along the axial direction, and both superconducting layers are modeled as perfect diamagnets. (Left) Cross-sectional spatial distribution of the magnetic flux density within the shield geometry. (Right) Profile of the magnetic field magnitude evaluated along the central axis of symmetry, corresponding to the path indicated by the black arrow in the left panel. The gray shaded region delineates the physical location of the sample volume.

Figure 4.6 presents a simulation of the multilayered screen subjected to a 100 mT external axial field, with the resulting magnetic field profile along the central axis plotted on the right. In the vicinity of the sample volume, the residual field drops below the 100 nT threshold, successfully achieving the targeted attenuation factor of 10^6 (or 120 dB).

Simulating transverse or off-axis magnetic fields is a much complex task. The necessity of a full 3D simulation not only increases computational complexity but also undermines solver convergence. This difficulty primarily came from the extreme aspect ratios of the mesh elements within the thin shielding layers, which yield an ill-conditioned system matrix. To overcome this, COMSOL's built-in *Magnetic Shielding* boundary condition was used. This feature replaces the volumetric bulk of the thin shells with an effective 2D surface boundary, completely circumventing the need to explicitly mesh the interior volume of the layers. This geometric simplification provides a substantial computational speedup.

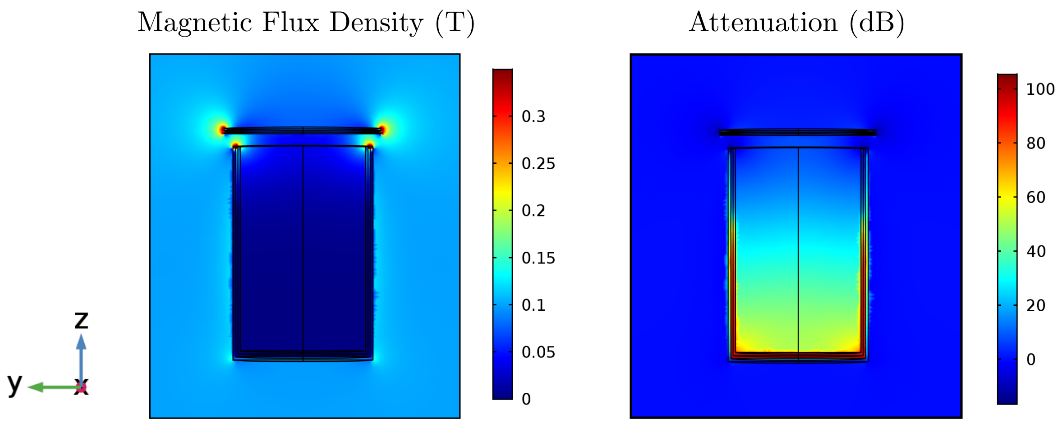

Figure 4.7: Full 3D simulation in COMSOL Multiphysics of the magnetic flux density (Left) and attenuation (Right) for an external magnetic field $B_0 = 100$ mT oriented along the y axis.

Figure 4.7 illustrates the 3D simulation of the shield subjected to a 100 mT external field oriented along the transverse y-axis. Even with these approximations, the 3D model remains computationally demanding, typically requiring several hours to converge. The attenuation results are noticeably worse than those observed in the axial case. This degradation occurs because the gap between the lid and the cylindrical layers allow transverse magnetic flux to penetrate the shielded volume more easily.

Low field operation

Not all experiments are conducted in high-magnetic-field environments; in many cases, shielding against the ambient Earth's magnetic field ($\sim 50\ \mu$T) is sufficient. The shield architecture was designed to be highly modular, allowing individual layers to be removed independently based on specific experimental requirements. For low-field applications, the SnPb and steel layers can be safely omitted. As showed in Figure 4.8, the remaining layers easily achieve a residual field well below the 1 nT threshold. This configuration also offers the possibility of reducing the overall height of the shield, facilitating its integration into more compact cryostat geometries, and accelerating the cooldown process because of the reduced mass.

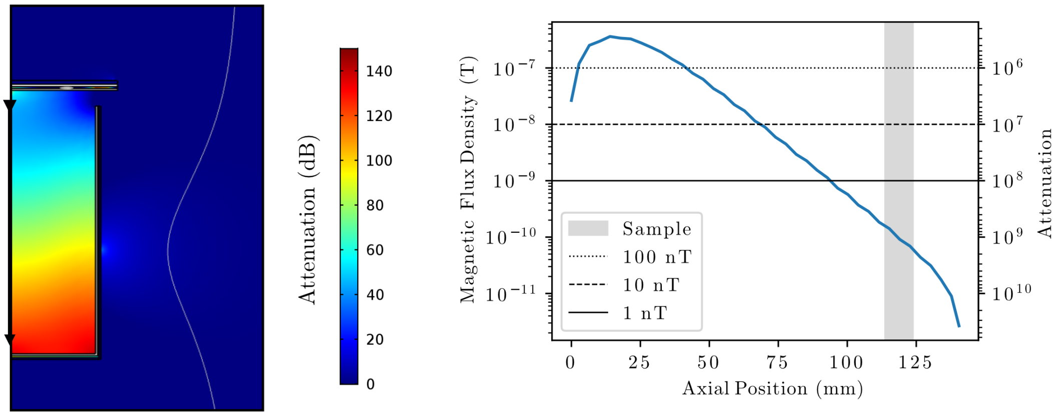

Figure 4.8: 2D axisymmetric magnetostatic simulation performed using COMSOL Multiphysics. A uniform external field of $B_0 = 50\ \mu$T is applied along the axial direction, and both superconducting layers are modeled as perfect diamagnets. (Left) Cross-sectional spatial distribution of the magnetic flux density within the shield geometry. (Right) Profile of the magnetic field magnitude evaluated along the central axis of symmetry, corresponding to the path indicated by the black arrow in the left panel. The gray shaded region delineates the physical location of the sample volume.

Room-temperature operations

As previously discussed, it is important to attenuate the ambient Earth's magnetic field even at room temperature to prevent initial flux trapping as the system cools through the superconducting transition. Figure 4.9 presents a simulation of the full shield stack under room-temperature conditions. In this regime, the superconducting layers are completely inactive and provide no shielding contribution.

The simulation results indicate only minimal attenuation from the outer steel layer, primarily due to the saturation. Conversely, the inner Cryoperm layer proves highly effective. Benefiting from the pre-attenuation provided by the steel and the multiplicative shielding effect between the nested layers. Even if residual magnetic flux were to become trapped within the Type II superconductor during cooldown, the Cryoperm layer acts as an optimal secondary shield, protecting the innermost Al layer.

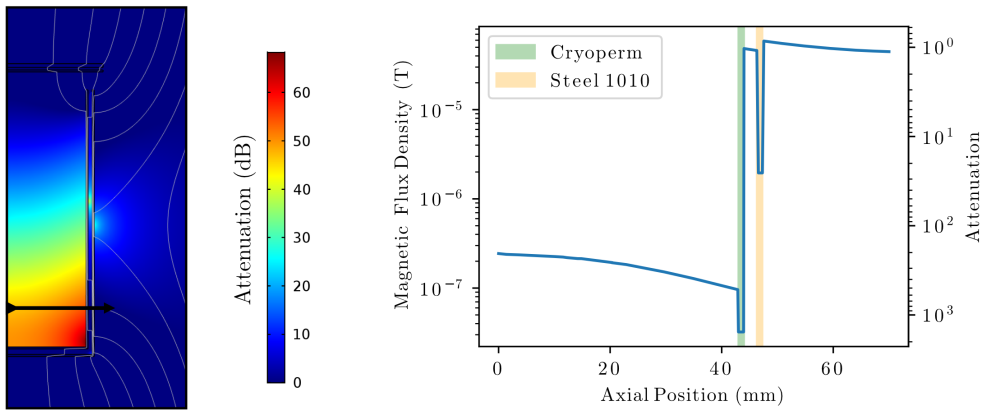

Figure 4.9: 2D axisymmetric magnetostatic simulation performed using COMSOL Multiphysics. A uniform external field of $B_0 = 50\ \mu$T is applied along the axial direction, because we are at room-temperature, the superconducting layers are inactive. (Left) Cross-sectional attenuation within the shield geometry. (Right) Profile of the magnetic field magnitude evaluated radially in proximity of the sample holder. The shaded regions delineates the physical location of the ferromagnetic layers.

Eddy current dissipation

During the magnetic field ramp following a zero-field cooldown, induced eddy currents primarily dissipate heat within the outermost ferromagnetic layer of the shield. To quantify this effect, the volumetric loss density across the material was integrated during a simulated linear field ramp of 1 mT/s. The calculated transient power dissipation remains strictly below 1 μW. This minor heat load adds to the baseline thermal dissipation of the mixing chamber plate and other internal cryostat components. Overall, this transient heat load is manageable and falls well within the typical 10 μW to 20 μW cooling power budget of standard dilution refrigerator operating at the 10 mK base stage.

4.4 Final considerations and shield validation

Due to manufacturing lead times, a comprehensive experimental validation of the magnetic shield could not be completed during the course of this internship. Nevertheless, rigorous empirical testing and characterization of the shield's magnetic properties remain essential to validate the numerical models and guide future design iterations. While the finite element simulations presented in the previous sections provide a solid foundation for the initial geometry, the inherent uncertainty regarding the exact magnetic properties of the selected alloys necessitates experimental verification. As discussed in Section 4.1.3, ferromagnetic materials can exhibit highly variable characteristics depending on their prior thermal and mechanical treatments, leading to unpredictable performance in cryogenic environments.

To fully characterize the shielding efficacy, a testing protocol should be implemented. Initial assessments can be conducted at room temperature using Hall probe measurements to determine the baseline magnetic field attenuation provided by the outer ferromagnetic layers. Subsequently, measurements at cryogenic temperatures could be performed using SQUID magnetometry to quantify the sub-microtesla residual fields.

The highly modular architecture of the proposed shield allows for the systematic removal of individual components. By evaluating the system with varying shielding configurations, it is possible to isolate and characterize the specific magnetic attenuation provided by each layer. Acquiring this data will be beneficial for calibrating the material parameters within the simulation framework, reducing theoretical uncertainties, and optimizing future iterations of the device design.

5

Stray photons shielding

As discussed in Section 3.4.1, quasiparticle tunneling constitutes a primary decoherence channel in superconducting circuits, limiting the energy relaxation time T_1 and increasing the residual thermal populations. While quasiparticles are expected to be negligible at typical dilution refrigerator temperatures, experimental evidence consistently reveals a significant non-equilibrium population across various devices.

A leading physical mechanism responsible for this excess population is thought to be the absorption of stray infrared (IR) photons. When incident photons possess an energy exceeding twice the superconducting gap, they can break Cooper pairs and directly generate non-equilibrium quasiparticles. Although mitigation strategies can be implemented directly at the chip level, such as engineering the superconducting bandgap profile or utilizing vortices to trap quasiparticles, macroscopic environmental shielding remains a necessity to block incident radiation before it reaches the device.

This chapter focuses on the design of such shielding mechanisms. The following sections will first detail macroscopic mitigation strategies, including the use of infrared-absorbing coatings, in-line microwave filters, and the mechanical design of a light-tight enclosure lid. Finally, to quantitatively evaluate the efficacy of these light-tightness measures, we will outline an experimental characterization method utilizing offset-charge-sensitive (OCS) transmon qubits.

5.1 Non-equilibrium quasiparticles

Building upon the formalism discussed in Section 2.3, the thermal quasiparticle fraction $x_{\mathrm{qp}}^{\mathrm{th}}$ can be estimated by integrating the superconducting density of states over the Fermi-Dirac distribution [45]. This yields an expression for the thermal contribution to the quasiparticle population at a given temperature T:

$$x_{\mathrm{qp}}^{\mathrm{th}} = \sqrt{2\pi \frac{k_B T}{\Delta}} e^{-\Delta/k_B T} \tag{5.1}$$

Assuming an aluminum-based superconducting circuit ($\Delta_{\mathrm{Al}} \approx 0.2$ meV) is in thermal equilibrium with the mixing chamber of a dilution refrigerator operating at 10 mK, the expected thermal population is vanishingly small (approximately 10^{-80}). However, experimental measurements consistently reveal a residual population on the order of 10^{-9} to 10^{-6}, corresponding to an effective quasiparticle temperature of approximately 100 mK [46].

The precise origin of these non-equilibrium, or *hot*, quasiparticles remains an area of active research. However, substantial evidence indicates that contribution on quasiparticle poisoning can be attributed to phonon burst [47], cosmic rays and environmental ionizing radiation [48, 49, 50], and especially stray infrared photons with energies exceeding twice the BCS gap ($2\Delta_{\mathrm{Al}} \gtrsim 100$ GHz) that can break Cooper pairs and increase the quasiparticle population x_{qp} [9, 51].

Regardless of the specific origin of these non-equilibrium excitations, the time evolution of the quasiparticle fraction x_{qp} can be phenomenologically described by a rate equation:

$$\frac{dx_{\mathrm{qp}}}{dt} = g - s x_{\mathrm{qp}} - r x_{\mathrm{qp}}^2 \tag{5.2}$$

where g represents the generation rate, s is the single-quasiparticle trapping rate, and r is the recombination rate at which two quasiparticles recombine into a Cooper pair. Various mitigation strategies to suppress the steady-state population have been implemented at the circuit level. A common approach is to enhance the trapping rate s through gap engineering [52, 53] or controlled vortex trapping [54]. Alternative designs incorporate normal-metal traps that allow quasiparticles to diffuse away from the junction, effectively introducing a spatial diffusion term into the rate equation [55].

This thesis focuses on minimizing the quasiparticle generation rate g through macroscopic shielding strategies. A primary contributor to g is infrared radiation propagating through transmission lines, stray photons originating from higher-temperature stages of the dilution refrigerator, and black-body radiation emitted by poorly thermalized microwave components such as attenuators and filters. In the following sections, we will analyze specific methodologies to block this incident infrared radiation and detail how these light-tightness measures are integrated into the overall shielding design.

5.2 Mitigation strategy against stray IR radiation

5.2.1 Infrared filters

The integration of infrared (IR) filters along all microwave transmission lines has become standard practice in superconducting circuit architectures [34]. The core requirement for an IR filter is near-zero insertion loss at the operational frequencies of the circuit (typically 4–8 GHz) while providing aggressive attenuation at higher frequencies ($>$ 20 GHz). To achieve this, many commercial filters (such as the YQuantum `YQ-IR-110A`) utilize Eccosorb CR-110 epoxy, which provide an attenuation scaling from approximately 5.4 dB/cm at 100 GHz up to 90 dB/cm at 1 THz. Because some of these absorptive epoxies contain magnetic particles whose performance can be degraded by strong external magnetic fields, they are optimally placed inside the innermost magnetic shield. Alternatively, filters employing non-magnetic, carbon-based absorbers (such as the Sweden Quantum `HERD2`) are immune to external magnetic field interference. Regardless of the chosen dielectric, all IR filters must be rigorously thermalized to the base temperature stage to ensure optimal absorptive performance and to prevent thermal emission.

5.2.2 Indium Seals and Stub Filters

The mechanical interface between the lid and the main cylinder body represents a critical vulnerability for stray photon ingress. To mitigate this, we employ two primary sealing strategies. First, the structural copper lid features a machined stub that protrudes into a corresponding mating groove on the main copper cylinder wall. This interlocking geometry acts as a labyrinth seal, highly attenuating high-frequency radiation. Future full-wave electromagnetic simulations of the S_{21} transmission parameter will be necessary to fully characterize and optimize this geometry. Second, to hermetically seal this labyrinth and ensure continuous electrical boundary conditions, a high-purity superconducting indium wire ring is compressed within the groove during assembly.

Another common leakage pathway is through structural fastener holes. To eliminate this, all mounting points on the primary inner copper shield utilize blind tapped holes, ensuring the wall thickness is never fully pierced. For instance, the *cold finger* supporting the sample holder is bolted to the inner face of the copper lid using screws anchored in blind threaded holes. This ensures excellent thermal contact without creating a line-of-sight radiation path into the shielded volume.

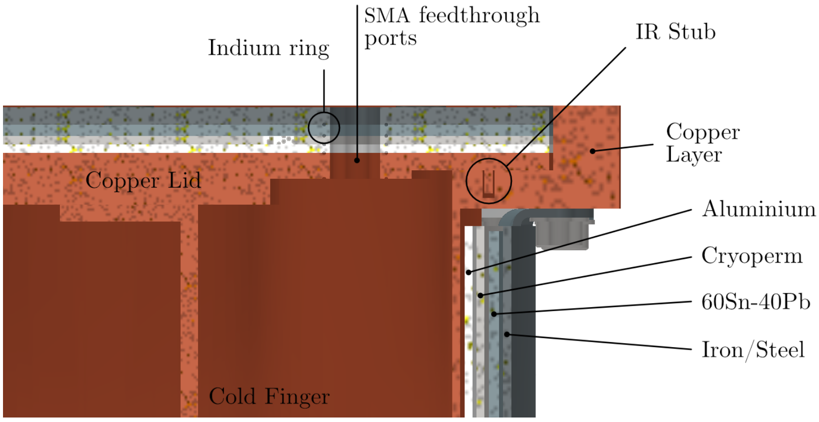

Figure 5.1: Cross section of the shield lid.

Finally, the system must interface with external microwave lines via SMA feedthrough ports that penetrate the entire multi-material layer stack of the lid. To prevent radiation from leaking radially into the shielded volume through the clearances between these nested layers, secondary indium wire gaskets are compressed around each SMA feedthrough at every layer interface, effectively blocking lateral light propagation.

5.2.3 IR-absorbing coating

A final preventative measure to control the quasiparticle population is the proactive absorption of any residual blackbody IR radiation that successfully enters or is generated within the shielded volume. This is accomplished by applying a highly absorptive coating to the interior surfaces of the shields. A compound consisting of silica, carbon powder, and silicon carbide

(SiC) grains provides broadband absorption of stray radiation. To minimize specular reflection of incoming IR photons and maximize absorption, the coating is applied such that its surface roughness is on the same order of magnitude as the target IR wavelengths [34].

5.3 Light-tightness characterization

Due to fabrication time constraints, an experimental validation of the manufactured shield was not possible within my internship activity. Consequently, this section outlines an experimental methodology to characterize the shield's effectiveness against Cooper pairs braking stray photons.

5.3.1 Offset Charge Sensitive qubits

As detailed in Chapter 3, quasiparticle tunneling events couple to the qubit degrees of freedom and degrade circuit performance. The effectiveness of the light-tightness strategies presented in this chapter can therefore be evaluated by measuring the quasiparticle tunneling rate. A preliminary approach to assess this shielding involves measuring the energy relaxation time T_1 of the qubit and comparing it with baseline measurements from previous, unshielded configurations. To introduce a controlled perturbation, a resistive filament can be mounted outside the shield; driving a current through this filament generates a black-body radiation source, enabling tests across different incident power levels. However, relying solely on T_1 is not completely rigorous, as qubit relaxation is simultaneously driven by a multitude of decoherence mechanisms.

A more precise method to isolate the shielding contribution is to directly analyze individual quasiparticle tunneling events at the Josephson junction. This is achieved by monitoring parity switches, which correspond to the tunneling of a single unpaired electron. To account for these events, the Hamiltonian from Equation 3.4 is modified to:

$$\hat{H} = 4E_C \left(\hat{n} - n_g + \frac{P-1}{4} \right)^2 - E_J \cos \hat{\varphi}, \tag{5.3}$$

where the parameter $P = \pm 1$ represents the even and odd charge parity states of the island respectively. Because the charge operator $\hat{n}$ is quantized in units of Cooper pairs ($2e$), a transition between the even and odd parity states shifts the effective offset charge by half a Cooper pair, signaling a single quasiparticle tunneling event. By continuously monitoring the parity of the qubit, one can build a direct record of quasiparticle tunneling.

As discussed in Section 3.2, the standard transmon regime exponentially suppresses sensitivity to offset charge. To experimentally distinguish between the even and odd parity bands, the qubit must be designed in an intermediate parameter regime between the Cooper-pair box and the transmon. This configuration, characterized by a ratio $E_J/E_C \sim 20$, is referred to as the offset-charge-sensitive (OCS) regime and is standard for probing quasiparticle populations in superconducting circuits [11, 51]. The energy levels of an OCS qubit for the even and odd parity states are plotted in Figure 5.2.

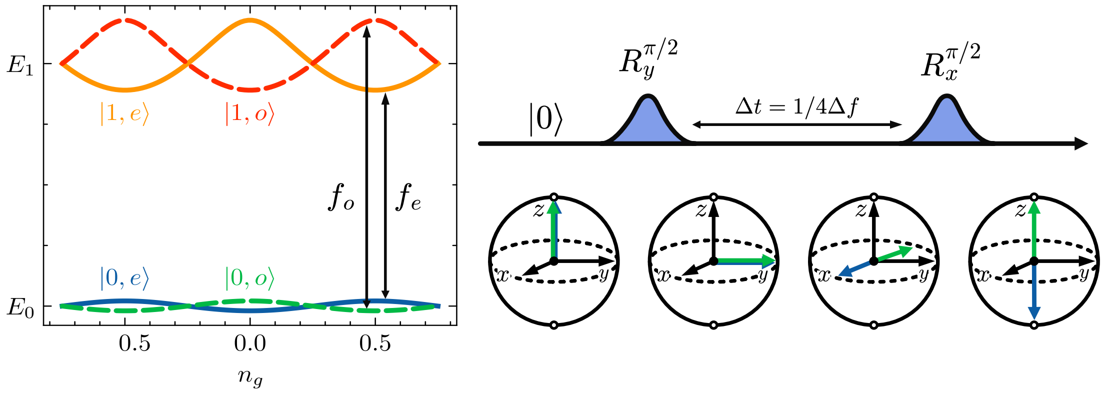

Figure 5.2: (Left) Energy level spectrum of an OCS qubit ($E_J/E_C = 10$) as a function of the gate-induced charge bias n_g. The transition frequencies between the ground and first excited states for the odd ($|0, o\rangle \rightarrow |1, o\rangle$) and even ($|0, e\rangle \rightarrow |1, e\rangle$) are denoted as f_o and f_e, respectively. (Right) Schematic of the Ramsey-like pulse sequence utilized to map the charge parity onto the state of the qubit.

The parity can be monitored in real time using a quantum non-demolition readout coupled with a specific Ramsey-like pulse sequence that maps the charge parity directly onto the qubit state [11]. As depicted in Figure 5.2, the sequence begins with a $\pi/2$ pulse applied along the y-axis, placing the qubit into the coherent superposition $(|0\rangle + |1\rangle)/\sqrt{2}$. The system is then allowed to idle for a duration $\Delta t = 1/(4\Delta f)$, where $2\Delta f = f_\mathrm{e} - f_\mathrm{o}$ is the frequency difference between the even and odd parity transitions. During this interval, the qubit state vector precesses around the z-axis of the Bloch sphere, accumulating a relative phase of $\pm\pi/2$ conditioned entirely on the parity state. A final $\pi/2$ pulse applied along the x-axis maps the odd parity state to $|1\rangle$ and the even parity state to $|0\rangle$.

Following the measurement, the qubit is conditionally reset, and the sequence is repeated. By fitting the power spectral density (PSD), the parity switching rate $\Gamma_{10}^{\mathrm{QP}}$ can be extracted. From this rate, the quasiparticle population x_{qp} is derived using Equation 3.10.

6

Measurement induced state transitions

While previous chapters focused on shielding against external factors like magnetic fields and stray photons, this chapter broadens the concept of *shielding* to address interactions between the quantum system and its control apparatus. Specifically, it investigates the detrimental effects of drive and readout pulses on the quantum state.

During dispersive readout, increasing the measurement photon number $\bar{n}$ improves the signal-to-noise ratio but simultaneously breaks down the approximations used to derive the dispersive Hamiltonian. As higher-order terms become significant, the measurement loses its QNDness [12]. This breakdown results in non-trivial couplings between transmon states at vastly different energy scales, driving spurious qubit excitations commonly referred to as measurement-induced state transitions (MIST).

To address this, a comprehensive simulation framework for a transmon coupled to arbitrary resonators is presented. By moving beyond the standard dispersive approximation, this tool determines the QND validity regime in advance. This allows for circuit design adjustments to avoid MIST, such as shifting operational frequencies or tuning auxiliary parameters like the gate charge bias n_g. Ultimately, this methodology provides a reliable strategy to *shield* the circuit from measurement-induced transitions and establish a safe operational parameter space.

6.1 Introduction

Before analyzing the spurious excitations of the qubit driven by multiphoton resonances, it is instructive to begin with the Jaynes-Cummings model. This two-level approximation, introduced in Section 3.3, provides closed-form solutions for concepts such as state dressing, avoided crossings, and hybridization, which will be essential in the following sections.

Recalling the Hamiltonian of Equation 3.7, we recognize the first two terms associated with the bare qubit $\hbar\omega_q\hat{\sigma}_z/2$ and the bare resonator $\hbar\omega_r\hat{a}^\dagger\hat{a}$. In the absence of the coupling term, parametrized by the constant g, the resulting *bare* states are simply the tensor product $|q,n\rangle$. In this two-level approximation, $q \in \{g,e\}$ denotes the state of the qubit, while $n \in \mathbb{N}$ represents the number of photons inside the cavity.

By activating the cavity-qubit interaction term, $\hbar g(\hat{a}^\dagger\hat{\sigma}_- + \hat{a}\hat{\sigma}_+)$, we allow for the coherent exchange of a single quantum between the qubit and the resonator. This interaction results in a *dressing* of the bare states, which can be computed analytically within the Jaynes-Cummings framework [22]. The resulting JC spectrum exhibits a block-diagonal structure where, for a fixed number of total excitations $\hat{a}^\dagger\hat{a} + \hat{\sigma}_+\hat{\sigma}_-$, the dressed eigenenergies and eigenstates are given by:

$$E_{\overline{g,n}} = \hbar n\omega_r - \frac{\hbar}{2}\sqrt{\Delta^2 + 4g^2 n}\,, \quad |\overline{g,n}\rangle = \cos\left(\frac{\theta_n}{2}\right)|g,n\rangle - \sin\left(\frac{\theta_n}{2}\right)|e,n-1\rangle$$
$$E_{\overline{e,n-1}} = \hbar n\omega_r + \frac{\hbar}{2}\sqrt{\Delta^2 + 4g^2 n}\,, \quad |\overline{e,n-1}\rangle = \sin\left(\frac{\theta_n}{2}\right)|g,n\rangle + \cos\left(\frac{\theta_n}{2}\right)|e,n-1\rangle$$

where $\Delta = \omega_q - \omega_r$ is the detuning between the bare qubit and resonator frequencies, and $\theta_n = \arctan(2g\sqrt{n}/\Delta)$. Depending on the value of Δ, the bare states begin to mix. At resonance ($\Delta = 0$), the dressed eigenstates become equal superpositions of the two bare states.

To quantify the degree of mixing between the states, we can define a hybridization metric, $\Theta(\lambda) = 1 - \left|\langle\lambda|\overline{\lambda}\rangle\right|^2$, based on the overlap between a bare state $|\lambda\rangle$ and its corresponding dressed state $|\overline{\lambda}\rangle$. As depicted in Figure 6.1, maximum hybridization occurs when the two states are in an equal superposition, yielding $\Theta(\lambda) = 0.5$. The coupling term $2g\sqrt{n}$ dictates the broadening of this hybridization, which is also evident in the avoided crossing of the energy levels: at zero detuning, the energy splitting between the two branches is $2g\sqrt{n}$.

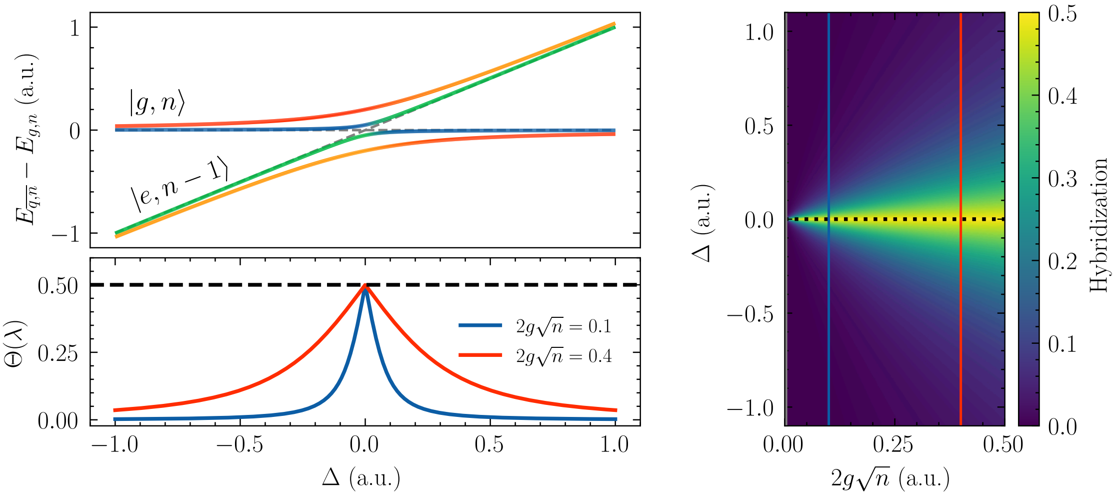

Figure 6.1: (Left) Avoided crossings of the dressed states eigenenergies for effective coupling strengths $2g\sqrt{n} = 0.1$ and 0.4. The lower panel displays the corresponding hybridization metric Θ swept across the resonance condition ($\Delta = 0$). (Right) A heatmap of the state hybridization as a function of frequency and effective coupling, demonstrating the increased broadening that occurs at stronger coupling strengths.

In the subsequent sections, we will move beyond the two-level approximation of the Jaynes-Cummings model to analyze how, and to what extent, the presence of cavity photons can trigger higher-order multiphoton processes. By extending the formalism discussed here, we will utilize the hybridization metric and the analysis of avoided crossings to track energy exchanges between a multilevel transmon and coupled resonators. Because additional effects such as Lamb shifts and AC-Stark shifts arise from the interaction of the multilevel transmon with the resonators, the simple hybridization features observed in Figure 6.1 will gain non-trivial contributions as multimode resonances occur. This approach will allow us to systematically analyze the spurious excitations that violate the dispersive approximation and compromise the fidelity of QND measurements.

6.2 Quantum model

Let us consider a system composed of a transmon qubit characterized by the Hamiltonian $\hat{H}_t$ from Equation 3.4. The transmon is coupled to N resonator cavities, each with a resonance frequency ω_k and a transmon-resonator coupling strength g_k. The combined resonator and interaction Hamiltonian takes the form:

$$\hat{H}_r + \hat{H}_{\text{int}} = \sum_{k=1}^{N} \omega_k \hat{a}_k^\dagger \hat{a}_k - i \sum_{k=1}^{N} g_k \left(\hat{n}_t - n_g\right) \left(\hat{a}_k - \hat{a}_k^\dagger\right) \tag{6.1}$$

Here, the LC oscillators and the transmon are capacitively coupled, similar to the Jaynes-Cummings Hamiltonian of Equation 3.7. However, because we want to study how the resonator fields induce spurious couplings between higher transmon levels, we avoid both the two-level approximation and the RWA.

To this system, we can apply a time-dependent drive, which could be either a readout tone directed at one of the resonators or an external pump applied directly to the transmon. A time-dependent drive with frequency ω_d and amplitude ε_d applied to the k-th resonator is described by the Hamiltonian:

$$\hat{H}_d(t) = -i\varepsilon_d \sin(\omega_d t) \left(\hat{a}_k - \hat{a}_k^\dagger\right) \tag{6.2}$$

In principle, the open-system dynamics can be simulated using a Lindblad master equation framework. This approach utilizes N Lindblad operators $\hat{L}_k = \sqrt{\kappa_k}\hat{a}_k$ to model the coupling between the quantum system and its external environment. Specifically, these operators capture the energy exchange with the outside world, accounting for the pumping and the dissipation of cavity photons at rate κ_k [56, 12]. This method is however computationally prohibitive because the required resources scale exponentially with the number of coupled modes. For instance, the total dimension of the system's Hilbert space is $\dim(\mathcal{H}) = D_t \times \prod_{k=1}^{N} D_k$, where D_t defines the truncation for the transmon energy levels, and D_k represents the maximum photon allowed in the Fock space of the k-th resonator.

For a transmon coupled to a single resonator, the authors of Reference [56] considered a Hilbert space dimension of 2^{15}, carrying out the simulation on Google's Tensor Processing Units (TPUs). More recent work [57] leverages tensor networks to efficiently simulate the same system, achieving a 10^5 reduction in required computational resources.

While tensor networks present a worthwhile path for future implementations, the present work focuses on analyzing how the presence of photons inside the resonators dresses the quantum states. By tracking these dressed states and identifying their correspondence with the bare states $|i_t; n_1, ..., n_N\rangle$ as the cavity photon number changes, we can observe the onset of hybridization. This is achieved by identifying avoided crossings between energy levels and observing population swaps between the excitations of the transmon and the resonators. This branch analysis [12] provides a robust framework capable of tracking MIST and other parametric processes occurring at the circuit level.

6.2.1 Branch analysis

The primary purpose of the branch analysis is to map the dressed eigenstates back to their corresponding uncoupled bare states. By tracking how these energy levels mix when the interaction is turned on, we can identify the nature of each hybridized state allowing to identify the states participating in the spurious excitations. The procedure is carried out through the following steps:

1. Initialization and diagonalization: We begin by considering the undriven, time-independent Hamiltonian $\hat{H} = \hat{H}_t + \hat{H}_r + \hat{H}_{\text{int}}$. By numerically diagonalizing this Hamiltonian, we obtain a set of dressed eigenstates $\{|\overline{\lambda}\rangle\}$.
2. Ground states identification: Next, we consider the resonator bare ground states $|i_t; 0_1, ..., 0_N\rangle$ derived from the uncoupled Hamiltonian $\hat{H} = \hat{H}_t + \hat{H}_r$ and identify the corresponding dressed eigenstate that maximizes the wavefunction overlap:
$$|\overline{i_t; 0_1, ..., 0_N}\rangle = \arg\max_{|\overline{\lambda}\rangle} |\langle\overline{\lambda}|i_t; 0_1, ..., 0_N\rangle|^2$$
3. Recursive state labeling: To label the higher-order dressed eigenstates, we recursively apply the creation operator $\hat{a}_k^\dagger$ for each k-th resonator and find the dressed wavefunction $|\overline{\lambda}\rangle$ that maximizes the overlap:
$$|\overline{i_t; n_1, ..., n_k + 1, ..., n_N}\rangle = \arg\max_{|\overline{\lambda}\rangle} |\langle\overline{\lambda}|\hat{a}_k^\dagger|\overline{i_t; n_1, ..., n_k, ..., n_N}\rangle|^2$$

This procedure is repeated until all relevant dressed states are labeled. Once the complete spectrum of dressed states is established, physical observables can be directly computed, such as the average transmon excitation N_t and the expected photon number N_k populating each resonator mode. Evaluating these observables clearly reveals the onset of coupling between states. For instance, the branch plot presented in Figure 6.2 tracks the transmon excitation N_t as a function of the increasing resonator population, explicitly indicating the cavity photon occupation levels at which specific spurious parametric processes occur.

The numerical diagonalization and subsequent branch analysis were implemented using JAX, a high-performance Python library. This framework allows for the efficient parallelization of linear algebra operations and code execution across CPUs, GPUs, and TPUs within a unified computational environment.

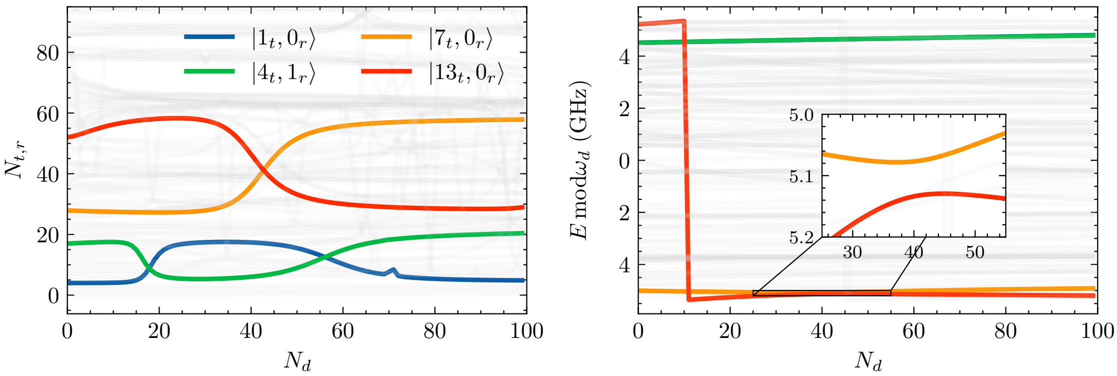

Figure 6.2: (Left) Branch analysis for a transmon ($E_J/h = 16.40$ GHz, $E_C/h = 0.1695$ GHz and $n_g = 0$) capacitively coupled to a spectator resonator ($\omega_r/2\pi = 9.029$ GHz) with a coupling strength $g_r/h = 0.153$ GHz. The transmon Hilbert space is truncated to the first $D_t = 31$ energy levels, while the spectator cavity to $D_r = 4$. A drive tone at $\omega_d/2\pi = 10.715$ GHz is applied to the transmon with a coupling $g_d = g_r$, and the drive is truncated to $D_d = 150$ photons. The branches are distinguished by the unique quantity $N_{t,r} = D_r N_t + N_r$, where N_r and N_t represent the average photon number and the transmon excitation, respectively. (Right) The dressed energy levels folded within the quasienergy interval $[-\omega_d/2, \omega_d/2]$. (Inset) A detailed view of the avoided crossing resulting from the coupling between the bare states $|7_t, 0_r\rangle$ and $|13_t, 0_r\rangle$.

To validate this numerical framework, the simulations are benchmarked against the experimental results reported in Reference [58]. Figure 6.2 presents the branch analysis of this driven transmon-resonator system, revealing several features. Notably, the transmon excited state $|1_t, 0_r\rangle$ couples to a higher-energy state $|4_t, 1_r\rangle$ via a six-wave mixing (6WM) process. In this multi-photon interaction, two drive photons are converted into three transmon excitations, promoting the transmon from $|1_t\rangle$ to $|4_t\rangle$, alongside the creation of a single photon in the spectator cavity. This 6WM process is dictated by the energy conservation condition, $\omega_{14} + 3\Delta_t^{\mathrm{ac}} + \omega_r = 2\omega_d$. The required energy is supplied by the drive and dynamically tuned by the

AC-Stark shift (Δ_t^{ac}), which is induced by a population of approximately 20 photons inside the drive resonator.

These parametric processes can be highly detrimental in experimental setups. For instance, attempting to measure the qubit in its excited state via standard dispersive readout can trigger a transition to the ionized state $|4_t\rangle$, even when the detuning between the qubit and the drive exceeds 6 GHz. The combination of AC-Stark shifts, multi-photon excitations, and inelastic scattering involving external modes can hybridize the circuit energy levels in a highly non-trivial way, breaking the QNDness of the measurement.

6.2.2 Hybridization and scar plots

Having established a formal framework to analyze specific transitions coupling different quantum states, it is convenient to evaluate the system over a broad parameter space, probing various drive frequencies and amplitudes. To quantify the degree of state mixing and generalize the onset of branch-swapping mechanisms, we extend the hybridization parameter Θ introduced in Section 6.1 as:

$$\Theta(\overline{\lambda}) = 1 - \max_{|\overline{\lambda}\rangle} \left| \langle \overline{\lambda} | \psi \rangle \right|^2 \tag{6.3}$$

To illustrate the physical meaning of this metric, consider a subspace spanned by two bare states, $|\lambda_1\rangle$ and $|\lambda_2\rangle$. A generic dressed state in this subspace can be expressed as $|\overline{\lambda}\rangle = \alpha |\lambda_1\rangle + \beta |\lambda_2\rangle$. In the far-detuned limit, the states do not hybridize (e.g., $|\overline{\lambda}\rangle \approx |\lambda_1\rangle$), the maximum overlap approaches $|\langle \lambda_1 | \overline{\lambda} \rangle|^2 = 1$, and therefore $\Theta(\overline{\lambda}) = 0$. Conversely, at exact resonance, the two bare states hybridize evenly, yielding the superposition $|\overline{\lambda}\rangle = (|\lambda_1\rangle \pm |\lambda_2\rangle)/\sqrt{2}$. In this maximally hybridized scenario, the overlap drops to 0.5, yielding $\Theta(\overline{\lambda}) = 0.5$.

By evaluating $\Theta(\overline{\lambda})$, one can construct a two-dimensional heatmap of the hybridization metric as a function of the drive frequency ω_d and the drive amplitude, which is parameterized by the average cavity photon number N_d. This visualization, presented in Figure 6.3, highlights regions in the parameter space where a target energy level undergoes strong hybridization. Because of the AC-Stark shift, the regions of maximal hybridization ($\Theta \approx 0.5$) manifest as curved trajectories across the parameter space. Due to their distinct visual appearance, these heatmaps are sometimes referred in the literature as *scar* plots [59].

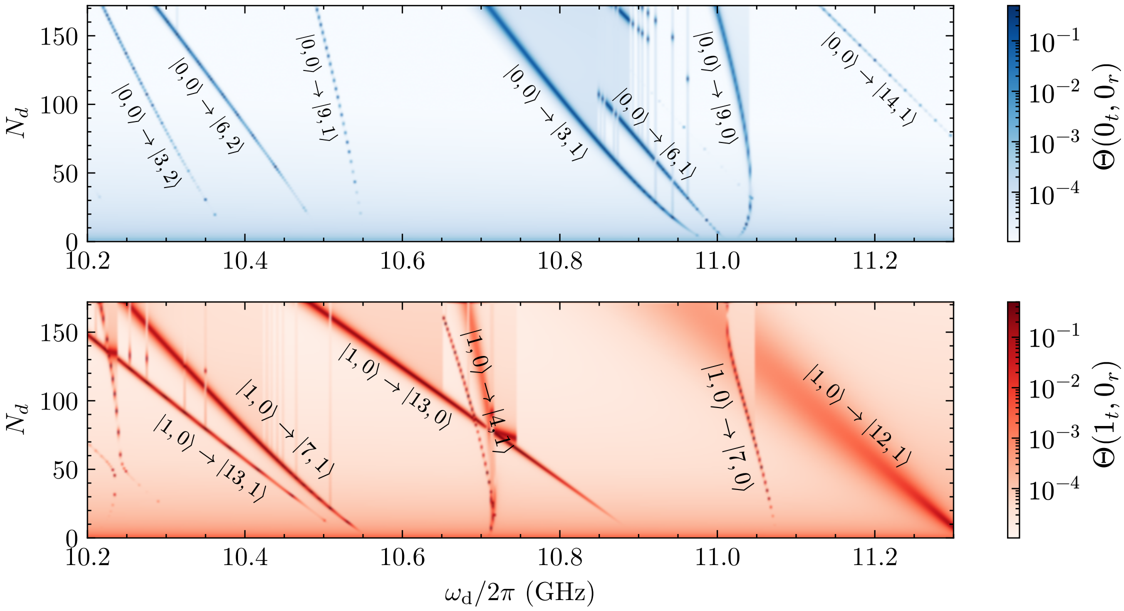

Figure 6.3: (Top) Hybridization of the bare ground state $|0_t, 0_r\rangle$. (Bottom) Hybridization of the excited state $|1_t, 0_r\rangle$. The system parameters are identical to those in Figure 6.2. The drive frequency $\omega_d/2\pi$ is swept across the interval $[10.2, 11.3]$ GHz using a grid of 500 samples, yielding results in good agreement with the Floquet analysis presented in Reference [58]. For this numerical simulation, the Hilbert space is truncated to $D_t = 15$ for the transmon and $D_r = 3$ for the resonator. The main *scars* are annotated with the specific bare state transitions that most closely correspond to the hybridized dressed states.

As illustrated in Figure 6.3, the hybridization metric is not perfect: certain artifacts arise from the mislabeling of bare states, which become increasingly pronounced at higher drive cavity photon populations. This difficulty is particularly evident for transitions to higher energy levels that exhibit a high degree of hybridization across multiple states. For this reason, a classical approximation can be employed for the drive field. This approach removes the constraint of a discrete photon number inside the drive resonator, enabling the implementation of more sophisticated branch-tracking techniques [60]. In the following section, this framework based on Floquet theory is briefly introduced and compared with the full quantum simulations.

6.3 Floquet simulation

An alternative to the full quantum model approximates the quantum drive of Equation 6.2 with a classical tone coupled directly to the transmon charge operator, $\hat{H}_d(t) \approx \Omega_d \cos(\omega_d t)\hat{n}_t$ [60, 12]. This eliminates the drive resonator and its large associated Fock space, drastically reducing the Hilbert space dimension. The classical amplitude Ω_d is connected to the quantum model via the average drive photon number N_d and coupling g_d, accordingly to $\Omega_d = 2g_d\sqrt{N_d}$.

Because this Hamiltonian is periodic with the drive period $T = 2\pi/\omega_d$, the system dynamics can be solved using Floquet theory. Analogous to Bloch's theorem in solid-state physics, Floquet's theorem dictates that any solutions to the time-dependent Schrödinger equation can be constructed from periodic Floquet modes, $|\phi_i(t+T)\rangle = |\phi_i(t)\rangle$, corresponding to the eigenvectors of the one-period time-evolution operator:

$$\hat{U}(t+T,t)\,|\phi_i(t)\rangle = e^{-i\epsilon_i T}\,|\phi_i(t)\rangle \tag{6.4}$$

where ϵ_i are the Floquet quasienergies, which are constrained to the first Floquet "Brillouin zone" $\epsilon_i \in [-\omega_d/2, \omega_d/2]$. Following diagonalization, the Floquet modes are analyzed similarly to the dressed states in the quantum branch analysis. In the zero-drive limit, the Floquet modes map exactly onto the bare states. By adiabatically increasing the drive amplitude, these states can be continuously tracked [12]. To more robustly identify multiphoton resonances and reproduce the hybridization metric from Equation 6.3, a polynomial fit of the state overlap across the drive amplitude-frequency parameter space can be performed. This fitting procedure constructs an ideal displaced Floquet mode $|\tilde{\phi}(t)\rangle$. Any deviation from this ideal state, quantified as $\Theta(\phi) = 1 - |\langle\tilde{\phi}|\phi\rangle|^2$, directly signals the onset of resonant processes [60, 58].

This method also allows the phenomenological inclusion of the drive cavity decay rate κ_d. By setting the amplitude sweep step proportional to the cavity rate ($\delta\Omega_d \propto \kappa_d$), the simulation accurately mimics Landau-Zener transition dynamics. A coarse step (representing a fast sweep or large κ_d) causes a diabatic transition that bypasses population swapping at narrow avoided crossings. Conversely, a finer mesh enables adiabatic following of the hybridized branches [12].

This Floquet-based framework was successfully employed in References [59, 58] using the Python library `floquet` [61]. The resulting simulations show good agreement with the full quantum models presented earlier. The primary advantage of the Floquet formalism lies in the significantly reduced Hilbert space, at the cost of the needs of performing sweeps over both the drive frequency ω_d and amplitude Ω_d, as well as the necessity to time-average observables over one drive period. Nevertheless, for more complex architectures, Floquet analysis provides a highly scalable and powerful tool. In the next section, this formalism is applied to probe parametric processes within a more complex quantum sensing device, specifically a Single Microwave Photon Detector (SMPD).

6.4 Case study: single microwave photon detector

In this final section, the single microwave photon detector (SMPD) [8, 62] is presented as a case study to analyze the parametric processes that enable its functionality, specifically the four-wave mixing (4WM) mechanism responsible for detecting single microwave photons. By employing the Floquet formalism, we will investigate the operational dynamics of the device and systematically analyze the drive- and measurement-driven transitions that can compromise its performance.

In its fundamental architecture, the SMPD comprises two resonators: a *buffer* mode (ω_b) and a *waste* mode (ω_w), both capacitively coupled to a central transmon qubit (ω_q). The detection protocol operates via 4WM, wherein an incident photon entering the buffer resonator is converted into a localized qubit excitation alongside a photon in the waste resonator [63]. This parametric conversion is actively triggered by an external pump tone applied at a frequency ω_p, satisfying the energy conservation relation $\omega_b + \omega_p = \omega_q + \omega_w$. Following this conversion step, a dispersive measurement of the qubit state is performed using the waste mode as a readout channel: detecting the transmon in its excited state signals the arrival of a photon in the buffer line. Finally, the qubit is reset to its ground state to repeat the detector cycle.

In physical implementations, the coupling between the qubit and the resonators makes the system susceptible to the Purcell effect, whereby the qubit can relax by emitting a photon into the external feedlines. To prevent these spurious qubit decays, the experimental device typically features secondary resonators acting as band-pass Purcell filters on both the buffer and waste lines [62]. For the sake of computational tractability, these Purcell filters are omitted from the simulations presented here. Future work will investigate whether their inclusion introduces relevant high-order effects to the parametric dynamics analyzed in the following sections.

During continuous operation, the presence of drive-induced unwanted state transitions (DUST) caused by multiphoton resonances from the pump tone, alongside MIST triggered during readout, can be highly detrimental. These spurious transitions disrupt both the measurement and reset protocols, increasing the dark count rate and degrading the detector's performance.

In the following paragraphs, the specific device architecture detailed in Reference [62] is analyzed to showcase the application of branch analysis and Floquet simulations to a complex system with practical utility. SMPDs are currently deployed in several experimental contexts, including the study of spin systems [1, 2] and the search for dark matter axions [6].

6.4.1 Tracking parametric processes

Following the experimental configuration detailed in Reference [62], the Floquet simulation is initialized with a qubit frequency $\omega_q/2\pi = 6.533$ GHz, a buffer resonator at $\omega_b/2\pi = 7.7$ GHz, and a waste resonator at $\omega_w/2\pi = 8.475$ GHz. Purcell filters are omitted in this simplified model. The effective cavity-transmon couplings are defined by the cross-Kerr shifts, $\chi_b/2\pi = 3.5$ MHz and $\chi_w/2\pi = 16$ MHz. The drive frequency $\omega_d/2\pi$ is swept from 7.20 to 7.30 GHz, with the drive amplitude parameterized by the induced AC-Stark shift Δ_q^{ac} [58]. The Hilbert space is truncated to $D_t = 11$ levels for the transmon and $D_r = 3$ photons for each resonator, though a more rigorous convergence analysis is warranted for future iterations. Simulations were executed using a custom modification of the `floquet` library.

Figure 6.4 displays the resulting *scar* plot, highlighting the ground state hybridization and focusing on the target states for 4WM dynamics: $|0_t, 1_b, 0_w\rangle$ and $|1_t, 0_b, 1_w\rangle$ (basis ordered as transmon, buffer, and waste). Both the branch analysis and the quasienergy spectrum resolve the avoided crossing between these states, directly confirming their resonant coupling. The *scar* plot reveals that as the pump amplitude increases, higher-order processes such as six- and eight-wave mixing begin to emerge. However, the quasienergy avoided crossings associated with these events are significantly narrower. Dictated by Landau-Zener adiabaticity conditions, the probability of these higher-order mixing transitions occurring remains small. Crucially, within this operational frequency range, no prominent spurious transitions are observed, which aligns with the relatively low pump-induced dark count rate $\alpha_{4\mathrm{wm}}$ measured experimentally [62].

Despite these insights, several open questions remain. The plot exhibits anomalous dark regions indicating exceptionally low state hybridization; it is currently unclear whether these features represent true physical suppression or are artifacts of the overlap metric and fitting

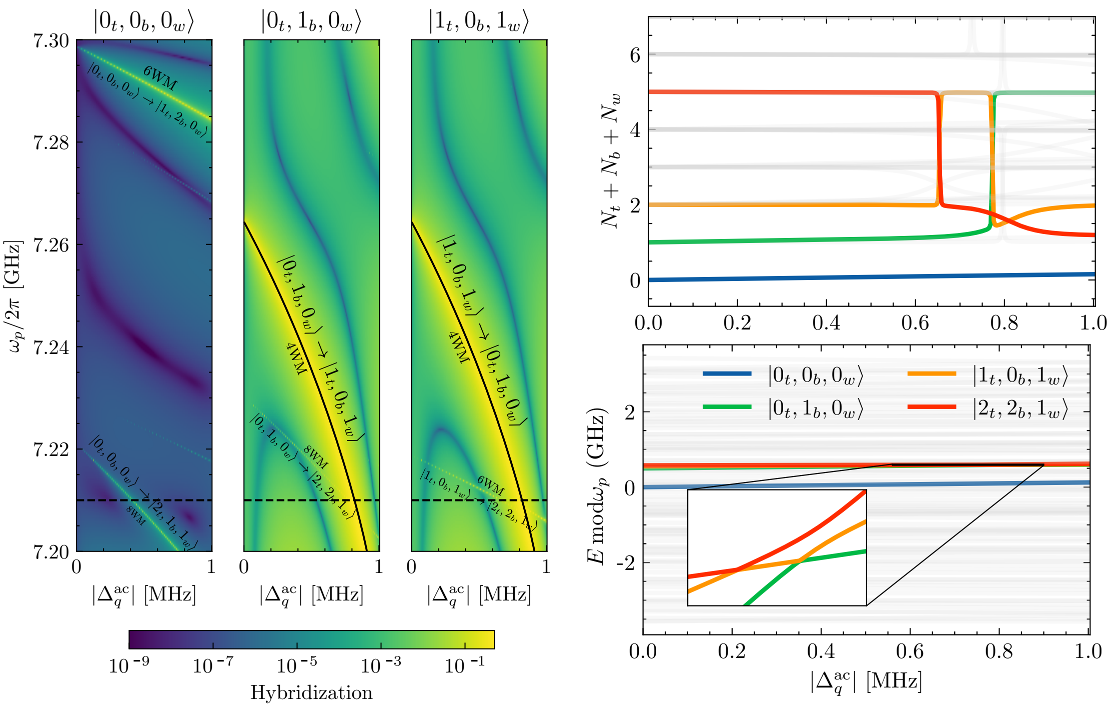

Figure 6.4: (Left) *Scar* plot illustrating the hybridization of the system ground state $|0_t, 0_b, 0_w\rangle$ and the primary states driving the mixing process. The 4WM trajectory is indicated by a solid black line, while higher-order processes are also annotated. The dotted black line shows the chosen pump frequency $\omega_p/2\pi = 7.21$ GHz used for the branch analysis. (Right) Branch analysis at $\omega_p/2\pi = 7.21$ GHz, revealing the onset of higher-order multi-photon processes as a function of pump amplitude.

procedure inherent to the Floquet formalism. Furthermore, the theoretical 4WM resonance condition is slightly detuned from the experimental value. This discrepancy likely stems from an overly aggressive Hilbert space truncation or an incomplete physical model, such as the omission of the Purcell resonators. To resolve these ambiguities, a completely rewritten Floquet simulation framework and further experimental validation are being pursued.

6.4.2 Tracking MIST

The analysis of MIST during the readout process is computationally simpler than the preceding analysis. In this scenario, the external pump tone is absent, and the readout field applied to the waste resonator is instead modeled as a classical drive within the Floquet framework. Consequently, the system configuration is analogous to the one analyzed in Section 6.3, comprising a single spectator resonator (the buffer mode) coupled to the transmon, with the readout field (the waste mode) acting directly as the drive.

This classical treatment of the readout field significantly reduces the dimensionality of the Hilbert space, as it eliminates the necessity of explicitly modeling the waste resonator as an additional quantized mode. To investigate the onset of MIST, a frequency sweep of this classical readout drive is performed across the interval $[8.4, 8.5]$ GHz. The resulting *scar* plot, presented in Figure 6.5, highlights the hybridization landscape and annotates the spurious state transitions occurring in the vicinity of the waste resonator frequency, $\omega_w/2\pi = 8.475$ GHz.

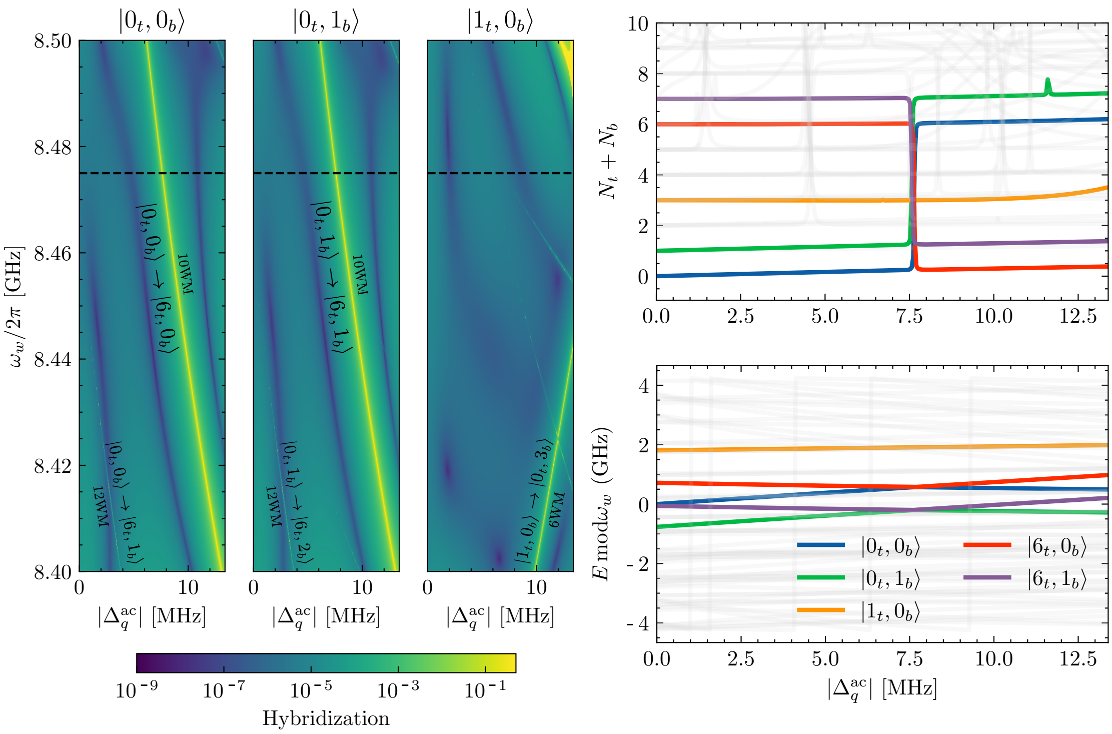

Figure 6.5: (Left) *Scar* plot illustrating the hybridization of the system ground state $|0_t, 0_b\rangle$ and the two primary states involved in the mixing process. The dotted black line indicates the frequency position of the waste resonator (readout) at $\omega_w/2\pi = 8.475$ GHz. (Right) The corresponding branch analysis is also shown.

In this simulation, the readout tone was probed at a substantially higher amplitude, reaching an AC-Stark shift of 12 MHz, which corresponds to a maximum population of approximately 50 photons within the waste resonator. At these high drive strengths, higher-order multiphoton processes begin to emerge. This includes a ten-wave mixing (10WM) process capable of ionizing the transmon, driving it directly from the ground state to the sixth excited state. However, similar to the findings in the parametric analysis, these high-order transitions exhibit weak coupling in the quasienergy spectrum. As a result, the standard operation of the dispersive readout remains largely safe from these highly suppressed spurious transitions, even at high photon number.

7

Conclusions

This thesis has investigated the comprehensive shielding of superconducting quantum circuits, addressing both ambient magnetic field interference and pair-breaking stray radiation. By combining high-permeability ferromagnetic layers with Type I and Type II superconductors, the proposed magnetic shield achieves a numerical attenuation factor exceeding 10^5. The highly modular and compact design ensures robust attenuation across different field and temperature regimes. The configuration provides effective magnetic shunting at room temperature, suppressing the ambient field before the superconducting transition and thereby mitigating the risk of flux trapping and subsequent dissipative effects. To support this design, a suite of magnetostatic finite element method simulations was developed, addressing the specific numerical challenges associated with modeling macroscopic superconducting domains. Furthermore, the cryogenic compatibility of the assembly was evaluated, confirming minimal eddy current dissipation and ensuring proper thermalization of all components.

In addition to magnetic isolation, a primary focus of this work was the establishment of strict light-tightness to protect the circuits from stray infrared photons. The absorption of these high-energy photons may generates non-equilibrium quasiparticles, which constitute a major decoherence channel in superconducting devices. To suppress this quasiparticle poisoning, several macroscopic mitigation strategies were implemented, including the geometric engineering the enclosure lid, the integration of absorptive foam, and the deployment of in-line microwave filters. Due to manufacturing time constraints, full experimental validation of the shield was not completed. Given the variability in the properties of magnetic alloys at cryogenic temperatures, future experimental testing using SQUID magnetometry is required to rigorously characterize the magnetic attenuation. Similarly, the light-tightness measures, such as the interlocking lid and stub design, must be validated through experimental quasiparticle tunneling measurements.

In the last chapter, the concept of shielding was extended to the interactions between the quantum system and its control and readout signals. The thesis analyzed how external drive and readout pulses can induce spurious qubit excitations, leading to a breakdown of the dispersive measurement regime. By employing a semi-classical Floquet framework, the behavior of a realistic quantum sensing device, specifically the SMPD, was successfully simulated. This analysis tracked the relevant parametric processes and identified the onset of measurement-induced state transitions triggered by the readout pulses. Future work will focus on improving this computational approach by developing a more performant Floquet simulation framework. Additionally, integrating tensor network methodologies presents a highly promising path to drastically reduce the Hilbert space dimensions, enabling the simulation of larger devices and more complex coupling architectures.

A

Derivations for magnetic shielding

A.1 Shielding with ferromagnetic materials

A.1.1 Analytical results for infinite cylinders

Let consider a infinite long cylinder of inner radius a and outer radius b made of a material with relative magnetic permeability μ_r. In the magnetostatic approximation, there is no current flowing, therefore $\nabla \times \mathbf{H} = 0$. This make more convenient to consider the magnetic scalar potential ψ defined by $\mathbf{H} = -\nabla\psi$. This make the Gauss law for the magnetic field be written as $\nabla^2\psi = 0$. Now, let consider a cross section of the cylinder, therefore we can work in polar coordinates (r, θ) and from separation of variables we find the relation of the magnetic potential as:

$$\psi(r,\theta) = \left(Ar + \frac{B}{r}\right)\cos\theta \tag{A.1}$$

where A and B are arbitrary constant. Now let consider the three regions inside the shield $r < a$, inside the material $a < r < b$ and on the outside $r > b$. Because of the constrain at $r = 0$ and $r \to \infty$, we are constrain on the choice of the constants. By requiring the continuity of ψ and its derivative $-\mu\, \partial\psi/\partial r$ (normal component of $\mathbf{B} = \mu\mathbf{H}$) at its boundaries $r = a$

and $r = b$, we recover the expression for the magnetic field in the interior of the shield:

$$B_{\text{int}} = \frac{4\mu_r B_0}{(\mu_r + 1)^2 - \eta^2(\mu_r - 1)^2} \tag{A.2}$$

where $\eta = a/b$. In the thin-shell approximation $t = b - a \ll a$ and then we can approximate $\eta^2 \approx 1 - 2t/a$, therefore the shielding factor, assuming high permeability materials $\mu_r \gg 1$, we can write the shielding factor as:

$$S = \frac{(\mu_r + 1)^2 - \eta^2(\mu_r - 1)^2}{4\mu_r} \approx \frac{\mu_r t}{2a} \tag{A.3}$$

A.1.2 Multiplicative effect

To analyze how multiple nested shields combine to yield a high total shielding factor, let us generalize the previous findings using a transfer matrix formalism. Consider a cylindrical interface at a radial position R_i separating two materials: an inner region i with permeability μ_i, and an outer region j with permeability μ_j. The state vectors defining the magnetic scalar potential in these two regions, evaluated at the interface, are $\mathbf{v}_i(R_i) = (A_i, B_i/R_i^2)^T$ and $\mathbf{v}_j(R_i) = (A_j, B_j/R_i^2)^T$.By imposing continuity of the scalar potential ψ and the normal magnetic flux density $\mu\,\partial\psi/\partial r$, we obtain the following relations:

$$A_i + \frac{B_i}{R_i^2} = A_j + \frac{B_j}{R_i^2} \qquad \mu_i\left(A_i - \frac{B_i}{R_i^2}\right) = \mu_j\left(A_j - \frac{B_j}{R_i^2}\right)$$

These equations can be rearranged into a matrix form by defining an interface matrix $\mathbf{M}_{ij}$, which transforms the state vector across the boundary from the outside medium to the inside medium:

$$\begin{pmatrix} A_i \\ B_i/R_i^2 \end{pmatrix} = \frac{1}{2}\begin{pmatrix} 1+\kappa_{ij} & 1-\kappa_{ij} \\ 1-\kappa_{ij} & 1+\kappa_{ij} \end{pmatrix}\begin{pmatrix} A_j \\ B_j/R_i^2 \end{pmatrix} \tag{A.4}$$

where we have defined the permeability ratio $\kappa_{ij} = \mu_j/\mu_i$. Symbolically, this boundary transformation is expressed as $\mathbf{v}_i(R_i) = \mathbf{M}_{ij}\mathbf{v}_j(R_i)$.

While $\mathbf{M}_{ij}$ solves a single boundary interface, a shield consists of layers of finite thickness. We must therefore propagate the state vector through a continuous material domain k from an outer radius r_{out} to an inner radius r_{in}. Because the coefficients remain constant within a homogeneous medium, we define a propagation matrix $\mathbf{P}(r_{\text{in}}, r_{\text{out}})$:

$$\begin{pmatrix} A \\ B/r_{\text{in}}^2 \end{pmatrix} = \begin{pmatrix} 1 & 0 \\ 0 & r_{\text{out}}^2/r_{\text{in}}^2 \end{pmatrix} \begin{pmatrix} A \\ B/r_{\text{out}}^2 \end{pmatrix} \tag{A.5}$$

Or symbolically, $\mathbf{v}_k(r_{\text{in}}) = \mathbf{P}(r_{\text{in}}, r_{\text{out}})\mathbf{v}_k(r_{\text{out}})$. A single shell layer is therefore characterized by a composite transfer matrix $\mathbf{T}_{layer}$ that combine the outer boundary, the internal bulk propagation, and the inner boundary:

$$\mathbf{T}_{\text{layer}} = \mathbf{M}_{\text{in}}\mathbf{P}(r_{\text{in}}, r_{\text{out}})\mathbf{M}_{\text{out}} \tag{A.6}$$

For a multi-layer shield, the complete system requires cascading all individual matrices along with the propagation matrices representing the free-space gaps between them. For a system of N concentric shells, the total transfer matrix $\mathbf{T}_{\text{tot}}$ is given by the following product:

$$\mathbf{T}_{\text{tot}} = \prod_{k=1}^{N} \mathbf{T}_k \mathbf{P}_{gap,k} \tag{A.7}$$

This total transfer matrix links the uniform external field to the field at the center of the shield. By applying the boundary condition that the field must remain finite at the origin, the total shielding factor is extracted directly from the upper-left matrix element $S_{\text{tot}} = (\mathbf{T}_{\text{tot}})_{11}$.

Two-layer shield

In the specific case of a two-layer shield, we can simplify the algebra by using the thin-shell ($t \ll a$) and high-permeability ($\mu_r \gg 1$) approximations. This allows to decompose each shell k in terms of its individual shielding factor, S_k.

The total transfer matrix is given by $\mathbf{T}_{\text{tot}} = \mathbf{T}_2\mathbf{P}(a_1, a_2)\mathbf{T}_1$, where $\mathbf{P}(a_1, a_2)$ crosses the vacuum gap from the inner shell (radius a_1) to the outer shell (radius a_2):

$$\mathbf{T}_{\text{tot}} = \begin{pmatrix} 1 + S_2 & S_2 \\ -S_2 & 1 - S_2 \end{pmatrix} \begin{pmatrix} 1 & 0 \\ 0 & a_1^2/a_2^2 \end{pmatrix} \begin{pmatrix} 1 + S_1 & S_1 \\ -S_1 & 1 - S_1 \end{pmatrix} \tag{A.8}$$

By isolating the upper-left element, we recover the total shielding factor:

$$S_{\text{tot}} \approx S_1 S_2 \left(1 - \frac{a_1^2}{a_2^2}\right) + S_1 + S_2 \tag{A.9}$$

A.2 Shielding with superconductors

A.2.1 Analytical results for perfect diamagnet

Following the derivation of the field attenuation for an infinitely long cylinder presented in the previous section, we can similarly determine the magnetic field behavior inside a superconducting cup. Consider a closed-bottom cylindrical shell subjected to an external axial field B_0. By employing the magnetic scalar potential ψ such that $\nabla^2\psi = 0$ we can solve Laplace's equation in cylindrical coordinates and enforce the zero-field boundary conditions at the superconducting walls. Assuming separation of variables, we decompose the potential as $\psi(r, z) = R(r)Z(z)$. Substituting this into the Laplace equation yields the following uncoupled ordinary differential equations:

$$\frac{\partial^2 Z}{\partial z^2} = k^2 Z \qquad \rho^2 \frac{\partial^2 R}{\partial \rho^2} + \rho \frac{\partial R}{\partial \rho} + \rho^2 R = 0 \tag{A.10}$$

where we have introduced the separation constant k and the radial coordinate change of variable $\rho = kr$. The general solution to the axial differential equation is $Z(z) = Ae^{+kz} + Be^{-kz}$, which can be equivalently expressed as $Z(z) = C \cosh k(z - z_0)$. Setting the open top of the cup at $z = 0$, and the closed bottom at $z = L$, and constraining the field to vanish at the base, we obtain $Z(z) = C \cosh k(L - z)$.

The radial differential equation takes the form of Bessel's equation, and its solution is the zeroth-order Bessel function of the first kind, $R(\rho) = J_0(\rho)$. Due to the Meissner effect, the normal component of the magnetic field at the internal wall of the cylinder $r = a$ has to be zero, therefore $J_0(ka) = 0$. Let $\alpha_1 \approx 2.405$ denote the first root of J_0. This determines our separation constant as $k = \alpha_1/a$. Consequently, the magnetic scalar potential inside the cylinder takes the form:

$$\psi(r, z) \propto J_0\left(\alpha_1 \frac{r}{a}\right) \cosh\left(\alpha_1 \frac{L - z}{a}\right) \tag{A.11}$$

By taking the gradient of the scalar potential, we recover the axial magnetic field component:

$$B_z(z) = \frac{B_0}{\sinh(\alpha_1 L/a)} \sinh\left(\alpha_1 \frac{L-z}{a}\right) \sim B_0 e^{-\alpha_1 z/a} \tag{A.12}$$

where B_0 is the applied field at the top opening of the cup. The exponential approximation holds true for aspect ratios where $L \gg a$.

B

Detailed Geometry and Dimensions

B.1 Shield dimensions

Based on the simulations and analysis presented in Chapter 4, the height of the innermost copper layer is set to 130 mm. The heights of the outer shielding layers are spaced in accordance with the thermal contraction constraints discussed in Section B.2, yielding a total base height of 140 mm. The top lid assembly adds an additional 15 mm to the overall vertical profile.

Figure B.1 illustrates the complete 3D design modeled in Autodesk Inventor. A cross-sectional view displays the full internal assembly, while panels (a) and (c) detail the lid structure using a false-color rendering to clearly distinguish the individual material components. The corresponding radial dimensions for each layer are summarized in Table B.1.

B.2 Thermal contraction

When cooling from room temperature to cryogenic temperatures, the materials of the shield undergo varying degrees of thermal contraction. The specific contraction values for the materials utilized in our assembly are detailed in Table B.2.

To accommodate this differential contraction between the inner copper core and the outer

Layer	Material	Inner diameter	Thickness	Gap after
0	Cu (OFHC)	80.0	1.0	0.5
1	Aluminium	83.0	1.0	0.5
2	Cryoperm	86.0	1.0	0.5
3	Lead-Tin	89.0	1.3	0.5
4	Steel 1010	92.6	1.0	–
	Outer diameter	**94.6**		

Table B.1: Radial dimensions expressed in millimeters for the diameter, thickness, and the gap between successive shells of the shield layers.

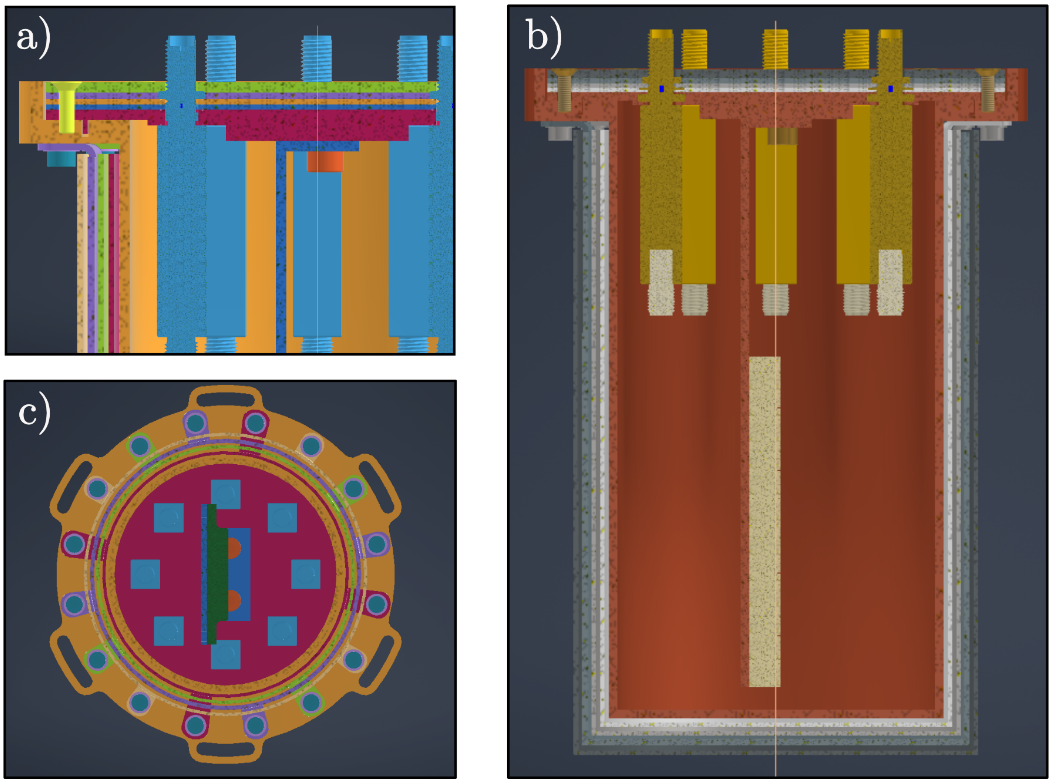

Figure B.1: Cross-sectional views of the complete shield assembly, equipped with HERD2 IR filters installed on the feedthrough ports. **(a)** and **(b)** present the axial cross-sections, while **(c)** displays a longitudinal cut detailing the underside of the lid and the mechanical layer interfaces. Panels **(a)** and **(c)** employ false-color rendering to clearly distinguish the individual material components.

shielding shells, a radial clearance of 0.5 mm is instituted between adjacent cylindrical layers. Because the absolute magnitude of contraction scales with dimension, the axial contraction along the height of the shield is more pronounced. Consequently, an axial spacing of 1.0 mm is maintained between the bottom caps of the nested layers.

Material	$\Delta L/L$ (300 K $\to$ 4 K)	**Contraction at** $r = 40$ **mm**
Copper	0.33%	0.13 mm
Aluminum	0.42%	0.17 mm
Lead	1.0%	0.40 mm
Steel / Cryoperm	$\sim$0.20%	$\sim$0.08 mm

Table B.2: Relative thermal contraction of shielding materials from 300 K to 4 K, and the corresponding absolute radial contraction for a typical layer radius of $r = 40$ mm.

At the mechanical interface between the shielding layers and the primary copper top lid, the design must ensure unconstrained dimensional changes while maintaining reliable thermal contact. To address this, the structural mounting interfaces feature radially slotted holes (see panel c of Figure B.1). This configuration allows the individual layers to slide radially during the cooldown process, effectively decoupling the stresses induced by differential contraction from the structural integrity of the assembly.

B.3 Thermalization

Proper thermalization of the shield is established through direct contact between the mixing chamber plate of the dilution refrigerator and the innermost copper layer. At millikelvin temperatures, thermal boundary resistance, governed by the Kapitza effect [64], requires minimizing the number of physical interfaces between dissimilar materials. The mechanical strategy used to manage thermal contraction concurrently provides a highly reliable thermal interface. Because each individual shielding layer is bolted directly to the primary copper structure (which is robustly anchored to the mixing chamber) rather than to adjacent shells, the design achieves a parallel thermalization path. This configuration offers significantly higher overall thermal conductance than a cascaded or series-connected architecture.

A strict design priority is the thermal anchoring of the sample holder. This is addressed using a dedicated cold finger bolted internally to the top copper lid, establishing direct, high-pressure contact with the main copper body. The exclusive use of copper-to-copper interfaces along this primary cooling path minimizes thermal impedance mismatches and maximizes boundary conductance. Furthermore, dedicated anchor points on the cold finger permit the attachment of flexible copper braids, ensuring that the infrared filters are adequately thermalized to the mixing chamber stage.

Acknowledgments

This thesis would not have been possible without the support, guidance, and encouragement of many individuals and institutions. First, I would like to express my gratitude to my internal supervisor, Prof. Caterina Braggio, and the University of Padova for their continuous support.

I am profoundly grateful to Patrice Bertet and the entire Quantronics group at CEA Paris-Saclay for providing me with this incredible internship opportunity and for welcoming me so warmly. I extend a special thank you to my external supervisor, Alexandre May, whose guidance, patience, and stimulating discussions kept me focused and motivated throughout the duration of the project.

Within the Quantronics group, I would like to specifically thank Leo Sutevski and Pasquale Mastrovito for their insightful discussions, suggestions, and the time they took to help me. I am also grateful to Alexandru Petrescu for his assistance in guiding me through the initial steps and theoretical framework of Chapter 6.

Finally, I would like to thank my family and friends for their continuous support throughout my studies.

References

[1] E. Albertinale, L. Balembois, E. Billaud, V. Ranjan, D. Flanigan, T. Schenkel, D. Estève, D. Vion, P. Bertet, and E. Flurin, "Detecting spins by their fluorescence with a microwave photon counter," *Nature*, vol. 600, no. 7889, pp. 434–438, 2021.

[2] Z. Wang, L. Balembois, M. Rančić, E. Billaud, M. Le Dantec, A. Ferrier, P. Goldner, S. Bertaina, T. Chanelière, D. Estève *et al.*, "Single-electron spin resonance detection by microwave photon counting," *Nature*, vol. 619, no. 7969, pp. 276–281, 2023.

[3] A. Chou, K. Irwin, R. H. Maruyama, O. K. Baker, C. Bartram, K. K. Berggren, G. Cancelo, D. Carney, C. L. Chang, H.-M. Cho, M. Garcia-Sciveres, P. W. Graham, S. Habib, R. Harnik, J. G. E. Harris, S. A. Hertel, D. B. Hume, R. Khatiwada, T. L. Kovachy, N. Kurinsky, S. K. Lamoreaux, K. W. Lehnert, D. R. Leibrandt, D. Li, B. Loer, J. Martínez-Rincón, L. McCuller, D. C. Moore, H. Mueller, C. Pena, R. C. Pooser, M. Pyle, S. Rajendran, M. S. Safronova, D. I. Schuster, M. D. Shaw, M. Spiropulu, P. Stankus, A. O. Sushkov, L. Winslow, S. Xie, and K. M. Zurek, "Quantum sensors for high energy physics," 2023. https://arxiv.org/abs/2311.01930

[4] H. Yi, S. C. Park, K. Kong, and M. Park, "High-frequency gravitational wave detection with superconducting qubits," 2026. https://arxiv.org/abs/2608.02733

[5] A. O. Sushkov, "Quantum science and the search for axion dark matter," *PRX Quantum*, vol. 4, p. 020101, May 2023. https://link.aps.org/doi/10.1103/PRXQuantum.4.020101

[6] C. Braggio, L. Balembois, R. Di Vora, Z. Wang, J. Travesedo, L. Pallegoix, G. Carugno, A. Ortolan, G. Ruoso, U. Gambardella, D. D'Agostino, P. Bertet, and E. Flurin, "Quantum-enhanced sensing of axion dark matter with a transmon-based single microwave photon counter," *Phys. Rev. X*, vol. 15, p. 021031, Apr 2025. https://link.aps.org/doi/10.1103/PhysRevX.15.021031

[7] P. Krantz, M. Kjaergaard, F. Yan, T. P. Orlando, S. Gustavsson, and W. D. Oliver, "A quantum engineer's guide to superconducting qubits," *Applied Physics Reviews*, vol. 6, no. 2, p. 021318, 06 2019. https://doi.org/10.1063/1.5089550

[8] L. Balembois, J. Travesedo, L. Pallegoix, A. May, E. Billaud, M. Villiers, D. Estève, D. Vion, P. Bertet, and E. Flurin, "Cyclically operated microwave single-photon

counter with sensitivity of $10^{-22}\ \mathrm{W}/\sqrt{\mathrm{hz}}$," *Phys. Rev. Appl.*, vol. 21, p. 014043, Jan 2024. https://link.aps.org/doi/10.1103/PhysRevApplied.21.014043

[9] M. Houzet, K. Serniak, G. Catelani, M. H. Devoret, and L. I. Glazman, "Photon-assisted charge-parity jumps in a superconducting qubit," *Phys. Rev. Lett.*, vol. 123, p. 107704, Sep 2019.

[10] C.-H. Liu, D. C. Harrison, S. Patel, C. D. Wilen, O. Rafferty, A. Shearrow, A. Ballard, V. Iaia, J. Ku, B. L. T. Plourde, and R. McDermott, "Quasiparticle Poisoning of Superconducting Qubits from Resonant Absorption of Pair-breaking Photons," Mar. 2022, arXiv:2203.06577 [quant-ph]. http://arxiv.org/abs/2203.06577

[11] D. Ristè, C. C. Bultink, M. J. Tiggelman, R. N. Schouten, K. W. Lehnert, and L. DiCarlo, "Millisecond charge-parity fluctuations and induced decoherence in a superconducting transmon qubit," *Nature Communications*, vol. 4, no. 1, May 2013. http://dx.doi.org/10.1038/ncomms2936

[12] M. F. Dumas, B. Groleau-Paré, A. McDonald, M. H. Muñoz-Arias, C. Lledó, B. D'Anjou, and A. Blais, "Measurement-Induced Transmon Ionization," *Physical Review X*, vol. 14, no. 4, p. 041023, Oct. 2024. https://link.aps.org/doi/10.1103/PhysRevX.14.041023

[13] H. Kamerlingh Onnes, "Further experiments with liquid helium. C. On the change of electric resistance of pure metals at very low temperatures etc. IV. The resistance of pure mercury at helium temperatures," *Koninklijke Nederlandse Akademie van Wetenschappen Proceedings Series B Physical Sciences*, vol. 13, pp. 1274–1276, 1911.

[14] W. Meissner and R. Ochsenfeld, "Ein neuer effekt bei eintritt der supraleitfähigkeit," *Naturwissenschaften*, vol. 21, p. 787–788, 1933.

[15] F. London and H. London, "The electromagnetic equations of the supraconductor," *Proceedings of the Royal Society of London. A. Mathematical and Physical Sciences*, vol. 149, no. 866, pp. 71–88, 1935. https://doi.org/10.1098/rspa.1935.0048

[16] M. Tinkham, *Introduction to superconductivity*, 2nd ed. Dover Publications, 2004.

[17] V. L. Ginzburg and L. D. Landau, "On the Theory of superconductivity," *Zh. Eksp. Teor. Fiz.*, vol. 20, pp. 1064–1082, 1950.

[18] A. A. Abrikosov, "The magnetic properties of superconducting alloys," *Journal of Physics and Chemistry of Solids*, vol. 2, no. 3, pp. 199–208, 1957. https://www.sciencedirect.com/science/article/pii/0022369757900835

[19] B. D. Josephson, "Possible new effects in superconductive tunnelling," *Physics Letters*, vol. 1, no. 7, pp. 251–253, 1962. https://www.sciencedirect.com/science/article/pii/0031916362913690

[20] J. Bardeen, L. N. Cooper, and J. R. Schrieffer, "Microscopic theory of superconductivity," *Phys. Rev.*, vol. 106, pp. 162–164, Apr 1957. https://link.aps.org/doi/10.1103/PhysRev.106.162

[21] B. Schumacher, "Quantum coding," *Phys. Rev. A*, vol. 51, pp. 2738–2747, Apr 1995. https://link.aps.org/doi/10.1103/PhysRevA.51.2738

[22] A. Blais, A. L. Grimsmo, S. M. Girvin, and A. Wallraff, "Circuit quantum electrodynamics," *Rev. Mod. Phys.*, vol. 93, p. 025005, May 2021. https://link.aps.org/doi/10.1103/RevModPhys.93.025005

[23] V. Bouchiat, D. Vion, P. Joyez, D. Esteve, and M. H. Devoret, "Quantum coherence with a single cooper pair," *Physica Scripta*, vol. 1998, no. T76, p. 165, jan 1998. https://doi.org/10.1238/Physica.Topical.076a00165

[24] J. Koch, T. M. Yu, J. Gambetta, A. A. Houck, D. I. Schuster, J. Majer, A. Blais, M. H. Devoret, S. M. Girvin, and R. J. Schoelkopf, "Charge-insensitive qubit design derived from the cooper pair box," *Phys. Rev. A*, vol. 76, p. 042319, Oct 2007. https://link.aps.org/doi/10.1103/PhysRevA.76.042319

[25] P. Kumar, S. Sendelbach, M. A. Beck, J. W. Freeland, Z. Wang, H. Wang, C. C. Yu, R. Q. Wu, D. P. Pappas, and R. McDermott, "Origin and Suppression of $1/f$ Magnetic Flux Noise," *Physical Review Applied*, vol. 6, no. 4, p. 041001, Oct. 2016, arXiv:1604.00877 [cond-mat.supr-con]. http://arxiv.org/abs/1604.00877

[26] C. Müller, J. H. Cole, and J. Lisenfeld, "Towards understanding two-level-systems in amorphous solids – Insights from quantum circuits," *Reports on Progress in Physics*, vol. 82, no. 12, p. 124501, Dec. 2019, arXiv:1705.01108 [cond-mat.mes-hall]. http://arxiv.org/abs/1705.01108

[27] G. Catelani, "Parity switching and decoherence by quasiparticles in single-junction transmons," *Phys. Rev. B*, vol. 89, p. 094522, Mar 2014. https://link.aps.org/doi/10.1103/PhysRevB.89.094522

[28] L. Glazman and G. Catelani, "Bogoliubov quasiparticles in superconducting qubits," *SciPost Phys. Lect. Notes*, p. 31, 2021. https://scipost.org/10.21468/SciPostPhysLectNotes.31

[29] K. Maki, "Fluxoid structure in superconducting films," *Annals of Physics*, vol. 34, no. 3, pp. 363–376, 1965.

[30] S. Posen, M. Checchin, O. Melnychuk, T. Ring, I. Gonin, and T. Khabiboulline, "High-quality-factor superconducting cavities in tesla-scale magnetic fields for dark-matter searches," *Phys. Rev. Appl.*, vol. 20, p. 034004, Sep 2023. https://link.aps.org/doi/10.1103/PhysRevApplied.20.034004

[31] B. D. Cullity and C. D. Graham, *Introduction to magnetic materials*. John Wiley & Sons, 2011.

[32] P. Oxley, J. Goodell, and R. Molt, "Magnetic properties of stainless steels at room and cryogenic temperatures," *Journal of Magnetism and Magnetic Materials*, vol. 321, no. 14, pp. 2107–2114, 2009, current Perspectives: Modern Microwave Materials. https://www.sciencedirect.com/science/article/pii/S0304885309000079

[33] M. Pentella, "Characterization of magnetic materials at extreme ranges of field," Ph.D. dissertation, Politecnico di Torino, 2022.

[34] E. I. Malevannaya, V. I. Polozov, A. I. Ivanov, A. R. Matanin, N. S. Smirnov, V. V. Echeistov, D. O. Moskalev, D. A. Mikhalin, D. E. Shirokov, Y. V. Panfilov, I. A. Ryzhikov, A. V. Andriyash, and I. A. Rodionov, "An engineering guide to superconducting quantum circuit shielding," *Applied Physics Reviews*, vol. 12, no. 3, p. 031334, Sep. 2025. https://pubs.aip.org/apr/article/12/3/031334/3364212/An-engineering-guide-to-superconducting-quantum

[35] L. Gozzelino, R. Gerbaldo, G. Ghigo, F. Laviano, M. Truccato, and A. Agostino, "Superconducting and hybrid systems for magnetic field shielding," *Superconductor Science and Technology*, vol. 29, no. 3, p. 034004, Mar. 2016. https://iopscience.iop.org/article/10.1088/0953-2048/29/3/034004

[36] C. Tain, "Modélisation des supraconducteurs de type II : implémentation avec FreeFem," Theses, Normandie Université, Dec. 2023. https://theses.hal.science/tel-04546205

[37] B. Dutoit, F. Grilli, and F. Sirois, *Numerical Modeling of Superconducting Applications*. World Scientific, 2023. https://www.worldscientific.com/doi/abs/10.1142/13282

[38] S. Farinon, G. Iannone, P. Fabbricatore, and U. Gambardella, "Numerical modeling of critical-state magnetization in type-ii superconducting cylinders under parallel and transverse magnetic field," *Cryogenics*, vol. 81, pp. 107–114, 2017. https://www.sciencedirect.com/science/article/pii/S001122751630056X

[39] C. Hickman, K. K. H. Leung, A. H. Al-Tawhid, B. W. Filippone, P. R. Huffman, E. Korobkina, D. P. Kumah, and C. M. Swank, "Superconducting properties of commercially available solders for low-field applications," 2025. https://arxiv.org/abs/2503.17345

[40] H. P. Langtangen and A. Logg, *Solving PDEs in Python*. Cham: Springer International Publishing, 2016. http://link.springer.com/10.1007/978-3-319-52462-7

[41] M. Olm, S. Badia, and A. F. Martín, "Simulation of high temperature superconductors and experimental validation," Apr. 2018, arXiv:1707.09783 [cs.CE]. http://arxiv.org/abs/1707.09783

[42] D. Meeker, *Finite Element Method Magnetics, Version 4.2*, 2015, user's Manual. http://www.femm.info

[43] I. A. Baratta, J. P. Dean, J. S. Dokken, M. Habera, J. S. Hale, C. N. Richardson, M. E. Rognes, M. W. Scroggs, N. Sime, and G. N. Wells, "DOLFINx: the next generation FEniCS problem solving environment," preprint, 2023.

[44] J. F. Fagnard, B. Vanderheyden, E. Pardo, and P. Vanderbemden, "Magnetic shielding of various geometries of bulk semi-closed superconducting cylinders subjected to axial and transverse fields," *Superconductor Science and Technology*, vol. 32, no. 7, p. 074007, Jul. 2019. https://iopscience.iop.org/article/10.1088/1361-6668/ab1824

[45] G. Catelani, R. J. Schoelkopf, M. H. Devoret, and L. I. Glazman, "Relaxation and frequency shifts induced by quasiparticles in superconducting qubits," *Physical Review B*, vol. 84, no. 6, Aug. 2011. http://dx.doi.org/10.1103/PhysRevB.84.064517

[46] K. Serniak, M. Hays, G. de Lange, S. Diamond, S. Shankar, L. D. Burkhart, L. Frunzio, M. Houzet, and M. H. Devoret, "Hot nonequilibrium quasiparticles in transmon qubits," *Phys. Rev. Lett.*, vol. 121, p. 157701, Oct 2018. https://link.aps.org/doi/10.1103/PhysRevLett.121.157701

[47] C. L. Chang, Y.-Y. Chang, M. Garcia-Sciveres, W. Guo, S. A. Hertel, X. Li, J. Lin, M. Lisovenko, R. Mahapatra, W. Matava, D. N. McKinsey, P. K. Patel, B. Penning, H. D. Pinckney, M. Platt, M. Pyle, Y. Qi, M. Reed, I. Rydstrom, R. K. Romani, B. Sadoulet, B. Serfass, P. Sorensen, B. Suerfu, V. Velan, G. Wang, Y. Wang, M. R. Williams, V. G. Yefremenko, and T. Collaboration, "Spontaneous generation of athermal phonon bursts within bulk silicon causing excess noise, low energy background events, and quasiparticle poisoning in superconducting sensors," *Applied Physics Letters*, vol. 127, no. 26, p. 263502, 12 2025. https://doi.org/10.1063/5.0281876

[48] M. McEwen, L. Faoro, K. Arya, A. Dunsworth, T. Huang, S. Kim, B. Burkett, A. Fowler, F. Arute, J. C. Bardin *et al.*, "Resolving catastrophic error bursts from cosmic rays in large arrays of superconducting qubits," *Nature Physics*, vol. 18, no. 1, pp. 107–111, 2022.

[49] A. P. Vepsäläinen, A. H. Karamlou, J. L. Orrell, A. S. Dogra, B. Loer, F. Vasconcelos, D. K. Kim, A. J. Melville, B. M. Niedzielski, J. L. Yoder *et al.*, "Impact of ionizing radiation on superconducting qubit coherence," *Nature*, vol. 584, no. 7822, pp. 551–556, 2020.

[50] L. Cardani, F. Valenti, N. Casali, G. Catelani, T. Charpentier, M. Clemenza, I. Colantoni, A. Cruciani, G. D'Imperio, L. Gironi *et al.*, "Reducing the impact of radioactivity on quantum circuits in a deep-underground facility," *Nature communications*, vol. 12, no. 1, p. 2733, 2021.

[51] S. Diamond, V. Fatemi, M. Hays, H. Nho, P. D. Kurilovich, T. Connolly, V. R. Joshi, K. Serniak, L. Frunzio, L. I. Glazman, and M. H. Devoret, "Distinguishing parity-switching mechanisms in a superconducting qubit," *PRX Quantum*, vol. 3, p. 040304, Oct 2022. https://link.aps.org/doi/10.1103/PRXQuantum.3.040304

[52] R.-P. Riwar and G. Catelani, "Efficient quasiparticle traps with low dissipation through gap engineering," *Phys. Rev. B*, vol. 100, p. 144514, Oct 2019. https://link.aps.org/doi/10.1103/PhysRevB.100.144514

[53] H. Nho, T. Connolly, P. D. Kurilovich, S. Diamond, C. G. L. Bøttcher, L. I. Glazman, and M. H. Devoret, "Recovery dynamics of a gap-engineered transmon after a quasiparticle burst," *Physical Review Letters*, vol. 136, no. 5, p. 050601, Feb. 2026, arXiv:2505.08104 [quant-ph]. http://arxiv.org/abs/2505.08104

[54] I. Nsanzineza and B. L. T. Plourde, "Trapping a single vortex and reducing quasiparticles in a superconducting resonator," *Phys. Rev. Lett.*, vol. 113, p. 117002, Sep 2014. https://link.aps.org/doi/10.1103/PhysRevLett.113.117002

[55] R.-P. Riwar, A. Hosseinkhani, L. D. Burkhart, Y. Y. Gao, R. J. Schoelkopf, L. I. Glazman, and G. Catelani, "Normal-metal quasiparticle traps for superconducting qubits," *Phys. Rev. B*, vol. 94, p. 104516, Sep 2016. https://link.aps.org/doi/10.1103/PhysRevB.94.104516

[56] R. Shillito, A. Petrescu, J. Cohen, J. Beall, M. Hauru, M. Ganahl, A. G. Lewis, G. Vidal, and A. Blais, "Dynamics of Transmon Ionization," *Physical Review Applied*, vol. 18, no. 3, p. 034031, Sep. 2022. https://link.aps.org/doi/10.1103/PhysRevApplied.18.034031

[57] A. Moulinas and X. Waintal, "A multilevel tensor network compression technique for simulating Lindblad dynamics in superconducting circuits," 2026, version Number: 1. https://arxiv.org/abs/2605.27515

[58] W. Dai, S. Hazra, D. K. Weiss, P. D. Kurilovich, T. Connolly, H. K. Babla, S. Singh, V. R. Joshi, A. Z. Ding, P. D. Parakh, J. Venkatraman, X. Xiao, L. Frunzio, and M. H. Devoret, "Characterization of Drive-Induced Unwanted State Transitions in Superconducting Circuits," *Physical Review X*, vol. 16, no. 1, p. 011011, Jan. 2026. https://link.aps.org/doi/10.1103/zdpg-mhpc

[59] A. V. Dixit, Z. L. Parrott, D. Chunikhin, B. Hauer, T. F. Q. Larson, and J. D. Teufel, "Millimeter Wave Readout of a Superconducting Qubit," Mar. 2026, arXiv:2603.13837 [quant-ph]. http://arxiv.org/abs/2603.13837

[60] X. Xiao, J. Venkatraman, R. G. Cortiñas, S. Chowdhury, and M. H. Devoret, "A diagrammatic method to compute the effective Hamiltonian of driven nonlinear oscillators," Dec. 2024, arXiv:2304.13656 [quant-ph]. http://arxiv.org/abs/2304.13656

[61] D. K. Weiss, "Floquet: Identifying nonlinear resonances in quantum systems due to parametric drives," https://github.com/dkweiss31/floquet, 2024.

[62] L. Pallegoix, J. Travesedo, A. S. May, L. Balembois, D. Vion, P. Bertet, and E. Flurin, "Enhancing the sensitivity of single-microwave-photon detection with bandwidth tunability," *Phys. Rev. Appl.*, vol. 25, p. 044064, Apr 2026. https://link.aps.org/doi/10.1103/dbqj-qld5

[63] R. Lescanne, S. Deléglise, E. Albertinale, U. Réglade, T. Capelle, E. Ivanov, T. Jacqmin, Z. Leghtas, and E. Flurin, "Irreversible qubit-photon coupling for the detection of itinerant microwave photons," *Phys. Rev. X*, vol. 10, p. 021038, May 2020. https://link.aps.org/doi/10.1103/PhysRevX.10.021038

[64] J. Chen, X. Xu, J. Zhou, and B. Li, "Interfacial thermal resistance: Past, present, and future," *Reviews of Modern Physics*, vol. 94, no. 2, p. 025002, Apr. 2022. https://link.aps.org/doi/10.1103/RevModPhys.94.025002